Liquid supersaturation in evaporating vertical falling films - A direct numerical simulation study

International Journal of Heat and Mass Transfer 255 (2026) 127760

Contents lists available at ScienceDirect

International Journal of Heat and Mass Transfer

journal homepage: www.elsevier.com/locate/hmt

Liquid supersaturation in evaporating vertical falling films — A direct numerical simulation study

D. Vleeschhouwers [a,*], N. Hidman [a], A. Åkesjö [b], H. Ström [a], S. Sasic [a]

[a] Department of Mechanics and Maritime Sciences, Chalmers University of Technology, Gothenburg, 41296, Sweden
[b] Södra, Väröbacka, 43286, Sweden

ARTICLE INFO

Keywords:
Two-phase DNS
Falling films
Evaporation
Supersaturation
VOF

ABSTRACT

Industrial fluids in heat exchanger applications frequently experience supersaturation, which can lead to crystallization and fouling on heat transfer surfaces, reducing system efficiency and performance. In this study, we investigate the roles of inverse salt solubility and interfacial evaporation, hypothesized to be the key mechanisms driving liquid supersaturation in evaporating vertical falling films. To identify where supersaturation first emerges and to elucidate the mechanisms behind its spatial distribution, a two-phase Direct Numerical Simulation (DNS) framework is developed that fully resolves hydrodynamics and heat transfer using a Volume of Fluid (VOF) approach. The gas–liquid interface is geometrically reconstructed to ensure accurate volume fraction and scalar flux calculations, with interfacial transport restricted to the liquid phase using a weighted scheme that avoids unphysical diffusion across the interface. A spatial segmentation method using periodic boundary conditions enables the simulation of an industrially relevant pipe length of 10 m within a compact computational domain. The framework is validated against prior numerical studies, experimental data, and analytical solutions, confirming its ability to capture the coupled hydrodynamic, heat, and mass transfer processes in the film. The results show that interfacial evaporation initiates supersaturation through solute enrichment near the gas–liquid interface, while flow separation and recirculation enhance supersaturation within the film. Supersaturation dynamics are strongly influenced by the Reynolds number (closely related to the wetting rate), with higher values leading to chaotic solute redistribution. Notably, supersaturation is consistently more pronounced near the bottom region of the evaporator, indicating a higher risk of crystallization fouling in this area.

1. Introduction

Falling liquid film evaporators are widely used in industrial processes requiring efficient heat and mass transfer, such as desalination, chemical processing, food production, pulp and paper manufacturing, and wastewater treatment. Their capability for high heat transfer rates combined with minimal thermal degradation makes falling film evaporators particularly suitable for handling temperature-sensitive liquids [1]. However, a significant operational challenge is fouling or scaling, characterized by undesirable crystalline deposits formed on heat-transfer surfaces due to local supersaturation, nucleation, and crystallization phenomena [2]. Fouling reduces heat transfer efficiency, increases pressure drops, and requires downtime for maintenance, leading to considerable economic losses in continuous industrial operations.

Crystallization fouling on heat transfer surfaces is fundamentally characterized by a sequential process that involves supersaturation, crystal nucleation, crystal growth, and subsequent deposition or removal at the heat transfer surface. Supersaturation is a necessary thermodynamic condition for crystallization fouling, as it governs both the nucleation of new crystalline deposits and the growth of existing ones. It arises when the solute concentration exceeds the equilibrium solubility limit, creating a metastable state that enables phase transition from dissolved species to solid crystal [3]. According to classical nucleation theory, stable nuclei formation spontaneously occurs once the concentration exceeds a critical supersaturation threshold [4]. In evaporating falling liquid films, the mechanisms driving supersaturation are not fully clear, thus warranting a detailed examination. We hypothesize that supersaturation predominantly arises through two distinct yet concurrent phenomena: inverse solubility of the salt, characterized by a decrease in solubility with increasing temperature [5], and solvent evaporation at the gas–liquid interface, which locally increases the solute concentration. While each mechanism independently facilitates supersaturation, their individual contributions and interactive effects

* Corresponding author.
E-mail address: denisvl@chalmers.se (D. Vleeschhouwers).

https://doi.org/10.1016/j.ijheatmasstransfer.2025.127760
Received 4 June 2025; Received in revised form 1 August 2025; Accepted 24 August 2025
Available online 5 September 2025

remain inadequately quantified and necessitate further rigorous investigation. Understanding the fundamental mechanisms underlying these driving forces of fouling is, therefore, of significant relevance to advance fouling mitigation strategies and optimize heat transfer efficiency.

While numerical studies of crystallization fouling have significantly advanced the modeling of general heat exchanger systems, the complex two-phase hydrodynamics specific to vertical falling films have received limited detailed treatment. Pääkkönen et al. [6] developed a mass deposition model that captures the kinematic properties of calcium carbonate ($CaCO_3$) fouling layers, which was later integrated with computational fluid dynamics (CFD) by Pääkkönen et al. [7] to simulate the growth of fouling by integration of solutes into existing layers. Extending the modeling to falling film conditions, Jin et al. [8] proposed a deposition-based approach for horizontal tube configurations, demonstrating the impact of film flow rates on fouling layer development. Azimifar et al. [9] focused specifically on vertical falling films, using a Lagrangian particle tracking framework to investigate the influence of particle size and inlet velocity on deposition behavior. These and other studies, including reaction-driven crystallization models, have significantly advanced our understanding of crystallization fouling. Additionally, Darand and Jafarian [2] examined long-term fouling in wastewater systems, confirming the dominance of surface integration processes. Together, these works provide valuable modeling strategies for industrial fouling scenarios. However, a detailed, mechanistic understanding of the hydrodynamic and transport phenomena that drive local supersaturation in vertical falling films remains limited. In most previous studies, supersaturated conditions were effectively imposed at the heat-transfer surface by prescribing initial and boundary conditions for salt concentration and temperature that reflect the presence of an existing fouling layer. In contrast, our approach does not assume any preexisting deposit; instead, supersaturation emerges naturally from the coupled transport processes within the liquid film. In this context, our work introduces a fully resolved two-phase hydrodynamic model of a vertical falling film, enabling the investigation of supersaturation as an emergent physical phenomenon that underpins crystallization fouling processes. By capturing the key transport processes that govern supersaturation in the film, we provide new insight into the early conditions that precede crystallization and fouling.

This study aims to identify where supersaturation first emerges within evaporating falling liquid films and to analyze how its spatial distribution is influenced by two key physical mechanisms: inverse solubility behavior and evaporation-driven solute accumulation at the gas–liquid interface. We systematically investigate how these mechanisms, individually and in combination, initiate supersaturation and subsequently drive the nucleation, crystallization, and fouling processes. Special emphasis is placed on understanding how the underlying fluid dynamics actively drives supersaturation by shaping the spatial–temporal evolution of solute concentration fields under conditions representative of industrial evaporating falling films. Gravitational, inertial, and surface tension forces generate complex fluid behaviors, including film thinning, wave formation, and hydrodynamic instabilities [10,11], which critically influence solute transport phenomena. Furthermore, we analyze the impact of varying Reynolds numbers on these processes. To achieve these objectives, we investigate the fundamental fluid dynamics and transport mechanisms underlying supersaturation using detailed two-phase Direct Numerical Simulations (DNS) based on the Volume-of-Fluid (VOF) method, explicitly resolving gas–liquid interfacial dynamics and incorporating evaporation effects at the gas–liquid interface. To capture the spatial evolution of key governing fields along the film flow in an evaporator of an industrial scale (10 m length), we devise a procedure for spatial segmentation of the unit, which makes it possible for us to identify the location of the onset of supersaturation and its spatiotemporal distribution in such a long unit. The solute transport is modeled with specialized numerical treatments to capture advective and diffusive processes, enabling localization of the onset of supersaturation. While previous studies have significantly advanced the understanding of fouling through reaction-based deposition models, our work complements these approaches by focusing on the fluid-dynamic mechanisms that drive supersaturation — a prerequisite for crystallization fouling. Rather than assuming pre-existing fouling conditions or prescribing simplified deposition kinetics, we simulate the full two-phase hydrodynamics of a vertical falling film to examine how transport and flow structures contribute to the local build-up of supersaturation. This approach provides valuable insights into the earliest stages of crystallization fouling and establishes a robust foundation for the development of predictive models and effective mitigation strategies for industrial falling-film evaporators.

2. Methodology

We investigate the fluid dynamics and transport mechanisms driving the formation of liquid supersaturation in evaporating vertical falling films over smooth heat transfer surfaces. Using two-phase direct numerical simulations, we resolve the coupling between hydrodynamics, heat transfer, and mass transport, including evaporation at the gas–liquid interface. Supersaturation is identified as a key precursor to crystallization fouling, arising from temperature-dependent solubility behavior (inverse salt solubility) and local solute enrichment due to evaporation. To quantify supersaturation within the liquid film, we introduce its mathematical definition [12]:

$$S(t,\mathbf{x}) = \frac{C_{salt}(t,\mathbf{x})}{C^{sat}_{salt}(T(t,\mathbf{x}))} \begin{cases} \text{Supersaturation} & \text{if } S(t,\mathbf{x}) > 1 \\ \text{Saturation} & \text{if } S(t,\mathbf{x}) \leq 1. \end{cases} \tag{1}$$

The scalar field $S(t,\mathbf{x})$ represents the local supersaturation at time t and position $\mathbf{x} = (x, y)$. A value of $S(t,\mathbf{x}) > 1$ indicates supersaturation, while $S(t,\mathbf{x}) \leq 1$ signifies a saturated or under saturated state. The term $C_{salt}(t,\mathbf{x})$ denotes the salt concentration, treated as a passive scalar in the liquid phase, while $C^{sat}_{salt}(T(t,\mathbf{x}))$ represents the temperature-dependent saturation concentration. For salts of inverted solubility, an increase in temperature $T(t,\mathbf{x})$ reduces $C^{sat}_{salt}(T(t,\mathbf{x}))$, lowering the solubility limit of the salt in the liquid. At elevated temperatures — particularly near the heat transfer surface — the solution of the system is pushed toward supersaturation because of its inverse soluble nature. Meanwhile, evaporation at the gas–liquid interface removes water, thereby locally increasing $C_{salt}(t,\mathbf{x})$, further driving supersaturation. This interplay between temperature-dependent solubility and interfacial evaporation is hypothesized to be a key driver of supersaturation and potential crystallization. Fig. 1 illustrates the falling liquid film, highlighting the gas–liquid interface and the critical thermal and concentration fields that govern the development of supersaturation under evaporative conditions.

To rigorously explore this hypothesis and capture the interactions driving these effects, a comprehensive numerical framework is needed. The numerical simulations are therefore conducted across a range of non-dimensional parameters that are essential for characterizing the complex interplay of hydrodynamics, heat, and mass transfer in gravity-driven falling films

$$Re = \frac{\Gamma}{\mu_l} = \frac{v_l h_l}{\nu_l}, \quad Ka = \frac{\sigma}{\rho_l \nu_l^{4/3} g^{1/3}}, \quad Pr = \frac{\nu_l}{\alpha_l},$$
$$Sc = \frac{\nu_l}{D_l}, \quad Ja = \frac{c_{p,l}(T_{wall} - T_{sat})}{h_{fg}}. \tag{2}$$

Eq. (2) defines several key dimensionless numbers that govern film dynamics through the interplay of fluid flow, heat- and mass transfer. The Reynolds number (Re) characterizes the relative importance of inertial forces to viscous forces, defined either by the wetting rate Γ and dynamic viscosity μ_l, or using the average film velocity v_l and thickness h_l in terms of the kinematic viscosity ν_l. The Kapitza number (Ka) quantifies the balance between surface tension and viscous-gravitational

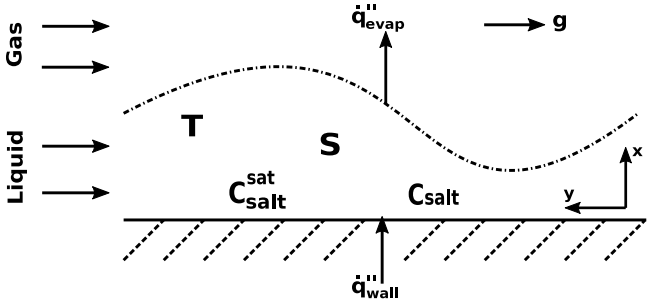

Fig. 1. Falling liquid film with a gas–liquid interface, illustrating the fields used to track and analyze the development of supersaturation regions S under evaporative conditions. Heat flux from the heated wall ($\dot{q}''_{wall}$) increases the local liquid temperature T, thereby reducing the solubility of the salt concentration C^{sat}_{salt} near the wall for inverse solubility systems. Simultaneously, evaporative heat flux at the interface ($\dot{q}''_{evap}$) leads to local enrichment of the solute concentration C_{salt}. Both effects lead to higher local supersaturation regions within the film. The figure is rotated 90 degrees counterclockwise for improved visualization.

forces, while the Prandtl (Pr) and Schmidt numbers (Sc) compare momentum diffusivity to thermal- (α_l) and mass diffusivity (D_l), respectively. The Jakob number (Ja) represents the ratio of sensible heat to latent heat during phase change, depending on the wall and saturation temperatures (T_{wall}, T_{sat}), the specific heat capacity $c_{p,l}$, and the latent heat of vaporization h_{fg}. The fluid properties appearing in these expressions include: ρ_l (density), σ (surface tension), α_l (thermal diffusivity), D_l (mass diffusivity of the salt in the solution), and $c_{p,l}$ (heat capacity). The gravitational acceleration is represented by g. The bulk gas velocity, v_g, is assumed to be sufficiently low — on the order of $O(10\ \mathrm{m/s})$ — relative to the bulk liquid velocity, v_l, such that its effect on the hydrodynamics of the liquid film is negligible [13]. Additionally, Åkesjö et al. [14] experimentally demonstrated that the circumferential flow components are negligible compared to the dominant wall-normal and vertical flow directions under the conditions relevant to this study. For simplification, the gas phase in the two-phase system is modeled using the thermophysical properties of air, treated as a passive medium. Additionally, atmospheric pressure is imposed uniformly throughout the entire computational domain. Based on these considerations, a two-dimensional approximation is adopted for the numerical framework and subsequent analyses.

In our simulations, black liquor was selected as the working fluid due to its inverse solubility properties and industrial relevance in the pulp and paper industry, where crystallization-induced fouling is a persistent challenge [15]. Based on the findings of Gourdon et al. [16], who showed that black liquor exhibits Newtonian behavior at the concentrations and temperatures relevant to this study, we model the fluid as Newtonian. This choice enables modeling a realistic setting, while the numerical framework remains adaptable to other fluids exhibiting similar supersaturation and crystallization behaviors, such as those encountered in the food industry [17]. The thermophysical properties of black liquor under evaporation conditions are modeled using experimentally derived correlations for the dynamic viscosity, density, thermal conductivity, and specific heat capacity

$$\mu_l = \mu_w 10^A, \quad A = \frac{\frac{\chi_s T^*}{T}}{0.679 - 0.656\frac{\chi_s T^*}{T}}, \tag{3}$$

$$\rho_l = 1007 - 0.495\,(T - 273.15) + 6\chi_s, \tag{4}$$

$$k_l = 0.00144\,(T - 273.15) - 0.335\chi_s + 0.58, \tag{5}$$

$$c_{p,l} = \left(1 - \chi_s\right) c_{p,w} + \chi_s c_{p,s} + c_{p,e}, \tag{6}$$

$$c_{p,e} = (4930 - 29\,(T - 273.15))\left(1 - \chi_s\right)\chi_s^{3.2} \tag{7}$$

where $T^* = 373$ K, $\mu_w = (36.6T - 10090)^{-1}$, $c_{p,w} = 4216$ J/kgK, $c_{p,s} = 1684 + 4.47\,(T - 273.15)$, and T, with temperature T in Kelvin. These correlations, reflecting the properties of sodium carbonate as a function of the dry solid content χ_s — the dominant inverse solubility salt in black liquor — serve as the basis for investigating supersaturation dynamics [18,19]. The sodium carbonate solubility, a key factor in determining the saturation concentration $C^{sat}_{salt}(T(t,\mathbf{x}))$, is highly temperature-dependent and is incorporated into our framework using a cubic polynomial fit

$$C^{sat}_{salt}(T(t,\mathbf{x})) = -0.0002268T^3(t,\mathbf{x}) + 0.04593T^2(t,\mathbf{x}) - 3.661T(t,\mathbf{x}) + 569. \tag{8}$$

This empirical correlation, based on solubility data from Shi [4], provides a precise means of tracking supersaturation dynamics under varying thermal conditions. The adaptability of the framework allows for substitution of this function for different working fluids, extending its applicability to diverse supersaturation and crystallization phenomena.

Having established the theoretical foundation, we next introduce the numerical framework employed to model these phenomena. This is followed by a grid independence study aiming at motivating our chosen degree of resolution of all relevant phenomena, and a validation of the framework against existing numerical, experimental and analytical solutions.

2.1. Numerical framework

A Volume-of-Fluid (VOF) method is employed to perform direct numerical simulations (DNS) of fully resolved hydro- and interfacial dynamics in falling films. VOF methods, both algebraic [20,21] and geometric [13,22], have been extensively used and validated in this field. Before introducing the governing equations, we first non-dimensionalize all variables using the liquid kinematic viscosity ν_l, liquid density ρ_l, and gravitational acceleration g, which together define the viscous, time, and velocity scales governing the flow

$$t^\Theta = \frac{t}{\left(\frac{\nu_l}{g^2}\right)^{\frac{1}{3}}}, \quad \mathbf{x}^\Theta = \frac{\mathbf{x}}{\left(\frac{\nu_l^2}{g}\right)^{\frac{1}{3}}}, \quad \mathbf{u}^\Theta = \frac{\mathbf{u}}{\left(\nu_l g\right)^{\frac{1}{3}}},$$

$$\mathbf{g}^\Theta = \frac{\mathbf{g}}{g}, \quad \rho^\Theta = \frac{\rho}{\rho_l}, \quad \nu^\Theta = \frac{\nu}{\nu_l},$$

$$p^\Theta = \frac{p}{\rho_l g\left(\frac{\nu_l^2}{g}\right)^{\frac{1}{3}}}, \quad \kappa^\Theta = \frac{\kappa}{\left(\frac{g}{\nu_l^2}\right)^{\frac{1}{3}}}, \quad \delta^\Theta = \frac{\delta}{\left(\frac{g}{\nu_l^2}\right)^{\frac{1}{3}}},$$

$$T^\Theta = \frac{T - T_{sat}}{T_{wall} - T_{sat}}, \quad C^\Theta_{salt} = \frac{C_{salt}}{\rho_l}. \tag{9}$$

The hydrodynamics of a falling film are primarily governed by the interplay of inertial, viscous, and capillary (surface tension) forces. While several approaches exist for non-dimensionalizing the governing equations, we adopt the conventional scaling widely used in the falling film community. Specifically, we employ the viscous length scale $\left(\nu_l^2/g\right)^{1/3}$ as the characteristic length scale. This scaling is used to non-dimensionalize key physical quantities - such as the velocity, pressure or spatial coordinates - in the conservation equations. The choice ensures consistency with established analyzes and facilitates comparison with previous studies in the field. In Eq. (9), the non-dimensional variables include the time t^Θ; spatial coordinates $\mathbf{x}^\Theta = \left(x^\Theta, y^\Theta\right)^T$; velocity $\mathbf{u}^\Theta = \left(u^\Theta, v^\Theta\right)^T$; gravitational acceleration $\mathbf{g}^\Theta = \left(g_x^\Theta, g_y^\Theta\right)^T$; density ρ^Θ; kinematic viscosity ν^Θ; pressure p^Θ; interface curvature κ^Θ; Delta-Dirac distribution function δ^Θ; temperature T^Θ; and salt concentration C^Θ_{salt} (equivalent to a mass fraction). Substituting these variables into the incompressible, two-phase Navier–Stokes equations leads to the following non-dimensional governing equations

$$\boldsymbol{\nabla}^\Theta \cdot \mathbf{u}^\Theta = 0, \tag{10}$$

$$\frac{\partial \mathbf{u}^{\Theta}}{\partial t^{\Theta}} + \nabla^{\Theta} \cdot (\mathbf{u}^{\Theta}\mathbf{u}^{\Theta}) = -\frac{1}{\rho^{\Theta}} \nabla^{\Theta} p^{\Theta} + \nabla^{\Theta} \cdot \left[\nu^{\Theta}(\nabla^{\Theta}\mathbf{u}^{\Theta} + (\nabla^{\Theta}\mathbf{u}^{\Theta})^{T})\right] + \mathbf{g}^{\Theta} + Ka\delta^{\Theta}\kappa^{\Theta}\mathbf{n}. \tag{11}$$

Eq. (10) represents the non-dimensional continuity equation, while Eq. (11) corresponds to the non-dimensional, conservative form of the two-phase momentum equation. The non-dimensional Nabla operator is given by $\nabla^{\Theta} = \left(\partial/\partial x^{\Theta}, \partial/\partial y^{\Theta}\right)^{T}$. The final term in Eq. (11) accounts for the additional acceleration due to surface tension σ at the phase interface. The Dirac-Delta distribution function, denoted as δ^{Θ}, is expressed in its non-dimensional form, scaled by the viscous length scale characteristic of the falling film. It represents the property of the surface tension force, which acts at the gas–liquid interface, and is non-zero only at this specific location. We emphasize that a different symbol, δ_N, is introduced later in the text to represent the non-dimensional film thickness. Despite the similar notation, δ_N is unrelated to the Dirac-Delta distribution δ^{Θ}. The interface unit normal vector $\mathbf{n}$ defines the geometrical orientation of the interface within a computational cell. To distinguish between the liquid and gas phases, the volume fraction transport equation is expressed in its conservative form

$$\frac{\partial f}{\partial t^{\Theta}} + \nabla^{\Theta} \cdot (\mathbf{u}^{\Theta} f) = 0, \tag{12}$$

where f represents the liquid volume fraction field, with $f = 1$ indicating the liquid phase and $f = 0$ denoting the gas phase. The gas–liquid interface is implicitly defined where $0 < f < 1$. Density and viscosity are discontinuous at the gas–liquid interface and are approximated with the arithmetic mean for the density, $\frac{\rho(f)}{\rho_l} = \rho^{\Theta}(f) = f + \frac{(1-f)}{\rho_r}$, and the harmonic mean for the dynamic viscosity, $\frac{\mu(f)}{\mu_l} = \mu^{\Theta}(f) = \left(f + (1-f)\mu_r\right)^{-1}$, where $\rho_r = \rho_l/\rho_g$ and $\mu_r = \mu_l/\mu_g$ are the density, respective dynamic viscosity ratios [23]. To account for thermal energy and salt concentration scalar transport in liquid and surrounding gas phase, we introduce their respective non-dimensional, conservative transport equations

$$\frac{\partial T^{\Theta}}{\partial t^{\Theta}} + \nabla^{\Theta} \cdot (\mathbf{u}^{\Theta} T^{\Theta}) = \nabla^{\Theta} \cdot \left(D^{\Theta}_{thermal}(\nabla^{\Theta} T^{\Theta})\right) + S^{\Theta}_{thermal}, \tag{13}$$

$$\frac{\partial C^{\Theta}_{salt}}{\partial t^{\Theta}} + \nabla^{\Theta} \cdot (\mathbf{u}^{\Theta} C^{\Theta}_{salt}) = \nabla^{\Theta} \cdot (D^{\Theta}_{mass}(\nabla^{\Theta} C^{\Theta}_{salt})) + S^{\Theta}_{mass}, \tag{14}$$

where $D^{\Theta}_{thermal}$ and D^{Θ}_{mass} are the non-dimensional thermal and mass diffusion coefficients, respectively, and $S^{\Theta}_{thermal}$, S^{Θ}_{mass} represent the source terms due to interface evaporation.

The governing equations (Eq. (10)–(14)) are solved using the open-source, finite-volume-based code Basilisk [24], which employs a quadtree-adaptive multigrid solver widely used for DNS of multiphase flows [13,25,26]. The computational domain is a two-dimensional square, discretized with a cell-centered tree-based adaptive mesh refinement scheme that dynamically refines or coarsens the grid. The non-dimensional domain size is given by L_{Box}/δ_N, where $L_{Box} = \delta_N s$, with the scaling factor s in our computations typically on the order of $O(100) - O(1000)$ and the non-dimensional Nusselt film thickness is defined as $\delta_N = (3Re)^{1/3}$ [27]. The incompressible two-phase Navier–Stokes Eqs. (10)–(11) are solved using an operator-splitting approach. First, an intermediate velocity field is computed without enforcing incompressibility. A pressure Poisson equation then ensures mass conservation, followed by a projection step to correct the velocity field. Time integration employs a second-order explicit staggered method for velocity and scalar fields [28]. Spatial advection of velocity and temperature in Eqs. (11) and (13) follows a flux-based, second-order, unsplit upwind scheme [28,29]. The volume fraction field (Eq. (12)) is advected using the Piecewise Linear Interface Calculation (PLIC) method, ensuring mass conservation and sharp interface representation [30,31]. At each time step t^n, the interface is reconstructed within each computational cell based on the volume fraction field of the previous step, $f(t^{n-1})$. The new volume fraction field $f(t^n)$ is computed using geometrically determined fluxes. To reflect the non-volatile nature of the dissolved salt, C^{Θ}_{salt} is defined to be zero in the gas phase and is strictly confined to the liquid, with no transport permitted across the gas–liquid interface. The interface is represented by the volume fraction field f, and both $\nabla^{\Theta} \cdot (\mathbf{u}^{\Theta} f)$ and $\nabla^{\Theta} \cdot (\mathbf{u}^{\Theta} C^{\Theta}_{salt})$ advection parts use the same geometrically conservative scheme. To prevent spurious scalar transfer at the phase boundary — a well-known numerical issue in multiphase flow simulations [32] — the advection of f and C^{Θ}_{salt} is performed synchronously. This numerical treatment of scalar advection avoids artificial relative motion between the scalar field and the interface, thereby eliminating non-physical mass leakage across the boundary and ensuring strict scalar conservation within the liquid phase [33,34]. Surface tension and pressure gradient in Eq. (11) are discretized using a well-balanced-force description to minimize spurious velocities at the gas–liquid interface and a height-function method is applied for accurate interface curvature estimation [35]. The time step Δt, constrained by the capillary time step [36], ensures the resolution of temporal and spatial capillary oscillations, in our simulations that typically range from $O(10^{-4})$ to $O(10^{-3})$.

The wall heat flux $\dot{q}''_{wall}$ increases the liquid temperature and may exceed the saturation temperature T_{sat}, inducing an evaporative heat flux $\dot{q}''_{evap}$ at the interface. Evaporation leads to cooling at the interface and in the gas phase and generates a non-divergence-free velocity field $\left(\nabla^{\Theta} \cdot \mathbf{u}^{\Theta} \neq 0\right)$ due to mass transfer [37]. However, we neglect this effect in Eqs. (10) and (13) for our falling film simulations, as the evaporation rate is typically negligible compared to the wetting rate Γ [38]. Consequently, the source term in Eq. (13) is modeled as a non-dimensional evaporative cooling term. A common approach for modeling evaporation in two-phase flow problems involving phase change is the Rankine–Hugoniot jump condition (Eq. (15)), which assumes no thermal resistance at the interface $\left(T_{l,int} = T_{g,int} = T_{sat}\right)$ [39]

$$\dot{q}''_{evap} = \dot{m}'' h_{fg} = k_g \nabla_{ng} T_g - k_l \nabla_{nl} T_l. \tag{15}$$

Here, $\dot{m}''$ represents the evaporation mass flux, h_{fg} is the latent heat of evaporation, and $\nabla_{ng} T_g$, $\nabla_{nl} T_l$ are the normal temperature gradients in the gas and liquid phases, respectively. This approach is well-suited for uniform Cartesian grids [40] but becomes challenging on an adaptive mesh, where dynamic resolution changes complicate normal temperature gradient calculations, particularly with stencil-based discretization [41]. To address this, our framework implements the evaporation model of Hardt and Wondra [42], incorporating evaporation as source terms at the interface in the governing equations. The evaporation mass flux is given by Eq. (16)

$$\dot{m}'' = \frac{T_{int} - T_{sat}}{R_{int} h_{fg}}, \tag{16}$$

where T_{int} is the interface temperature, and R_{int} represents the thermal resistance of the gas–liquid interface $\left(T_{int} \neq T_{sat}\right)$. Based on the considerations of Schrage [43], R_{int} is expressed with Eq. (17)

$$R_{int} = \frac{2-\alpha}{\alpha} \frac{\sqrt{2\pi R_g}}{h_{fg}^2} \frac{T_{sat}^{3/2}}{\rho_g}, \tag{17}$$

with α is the evaporation coefficient, R_g is the gas constant and ρ_g the gas density. Physically, the evaporation coefficient α governs the rate of phase change at the gas–liquid interface and is inversely related to the interfacial thermal resistance R_{int}, which characterizes the ability of heat to be transferred from the liquid bulk to the interface. In this study, we set $\alpha = 0.8$, a value within the typical range of 0 to 1, where $\alpha = 1$ corresponds to the theoretical maximum evaporation rate. In the limiting case $\alpha \to 0$ (or equivalently $R_{\text{int}} \to \infty$), the interface becomes highly resistive to thermal transport. Consequently, the supply of latent heat required for evaporation is restricted, which inhibits phase change and may result in local interfacial overheating. This condition can further elevate the gas-phase temperature adjacent to the interface, deviating from saturation and introducing unphysical behavior. To

accurately model the intended regime of efficient, saturation-controlled evaporation—where interfacial cooling dominates and the interface remains at the saturation temperature—we choose a relatively high value of α. This corresponds to the limit $R_{\text{int}} \rightarrow 0$, where thermal resistance is negligible and the latent heat of vaporization is readily supplied from the liquid phase. Under these conditions, phase change proceeds steadily and consistently with physical expectations, avoiding spurious thermal effects at the interface.

To localize the evaporation mass flux at the gas–liquid interface and obtain the local evaporation mass flux φ_{evap}, $\dot{m}''$ is scaled by the magnitude of the volume fraction gradient $\mid \nabla f \mid$, ensuring that the evaporation occurs only at the interface, $\varphi_{evap} = \dot{m}'' \mid \nabla f \mid$. The cooling term can thus be expressed as the product of the local evaporation mass flux and the latent heat of evaporation, yielding a volumetric source term $\dot{q}'''_{evap} = -\dot{q}''_{evap} \mid \nabla f \mid$ [42]. Incorporating $\dot{q}'''_{evap}$ into the non-dimensional framework results in

$$S^{\Theta}_{thermal} = -\frac{\mid \nabla f \mid^{\Theta}}{A^{\Theta}} T^{\Theta} \tag{18}$$

where A^{Θ} is the non-dimensional thermal resistance $A^{\Theta} = \rho_l c_{p,l} \left(\nu_l g\right)^{1/3} R_{int}$, and the negative sign accounts for energy removal due to evaporative cooling. The evaporation model is now applied to derive the non-dimensional source term S^{Θ}_{mass} in Eq. (14). The local evaporation mass flux accounts for the increase in C^{Θ}_{salt} within interface cells, which results from the decreasing water volume due to evaporation. This leads to the following expression

$$S^{\Theta}_{mass} = B^{\Theta} C^{\Theta}_{salt} T^{\Theta} \mid \nabla f \mid^{\Theta}, \tag{19}$$

where B^{Θ} is a non-dimensional factor $B^{\Theta} = Ja \left(A^{\Theta}\right)^{-1}$. The values $A^{\Theta} = 0.002$ and $Ja = 0.0151$ are determined based on the dry solid content χ_s, as introduced in Eqs. (3)–(6).

To capture the thermal and concentration scalar diffusive fluxes from the interface cells into adjacent liquid-phase cells, we implement a weighting method based on the analytically reconstructed interface [34]. This scheme modifies the effective diffusion coefficients at cell faces by incorporating the volume fraction at each cell face. For example, the mass diffusion coefficient (similarly for the thermal diffusion coefficient) is computed as $D^{\Theta}_{mass} = (D^{\theta}_{mass,eff})\varphi^f$ where $D^{\Theta}_{mass,eff}$ is an effective diffusion coefficient at the face, and φ^f is the face volume fraction of the considered interfacial cell. For the effective diffusion coefficient, we use the non-dimensional diffusion coefficient of the liquid, expressed as $D^{\Theta}_{mass,eff} = 1/Sc_{liq}$. The contribution of the gas-phase can be neglected, since $Sc_{gas} \ll Sc_{liq}$ for our application. This also applies to the effective thermal diffusion coefficient, since $Pr_{gas} \ll Pr_{liq}$. Fig. 2 illustrates an interface cell where the shaded region represents the liquid phase, and the white region denotes the gas phase. The dashed line marks the reconstructed interface, defining the face volume fractions. At fully immersed liquid faces (e.g. the left face in Fig. 2), $\varphi^{f,l} = 1$, ensuring that $D^{\Theta}_{mass} = D^{\Theta}_{mass,eff}$. For faces intersected by the interface, for example the top and bottom faces ($0 < \varphi^{f,b} < 1$ and $0 < \varphi^{f,t} < 1$), φ^f scales the diffusion coefficient, ensuring a physically consistent representation of diffusive fluxes from the interface cells into adjacent liquid-phase cells and also preventing scalar concentration transfer into the gas-phase. We emphasize that the symbol φ^f is intentionally chosen to denote the volume fraction evaluated at the face of a computational cell. Specifically, φ^f represents the fraction of the cell that is intersected by the analytically reconstructed interface line, aligned with either the vertical or horizontal cell face, depending on orientation. This definition is distinct from the commonly used volume fraction variable f, which refers to the cell-centered volume-averaged fraction of liquid within a computational cell.

To ensure consistency in the transport of the scalar at interfaces, particularly for discontinuities such as the salt concentration scalar C^{Θ}_{salt}, it is essential to distinguish between total volume-averaged and phase-averaged quantities. The total volume average represents the concentration scalar averaged over the total volume of the computational cell, encompassing both phases, whereas the phase average corresponds to the concentration scalar averaged exclusively over the volume of a specific phase within the cell, such as the liquid phase. Their mathematical formulations are given by

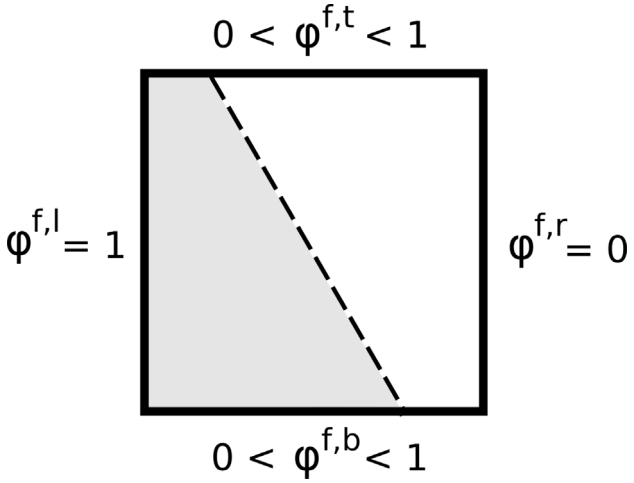

Fig. 2. Schematic representation of an interface cell with a reconstructed interface (dashed line). The shaded region represents the liquid phase, while the white region corresponds to the gas phase. The face volume fraction φ^f is determined based on the reconstructed interface geometry.

$$\langle C_{liq} \rangle_{V_{cell}} = \frac{1}{V_{cell}} \int_{V_{liq}} C_{liq} dV = \frac{V_{liq}}{V_{cell}} C_{liq} = f C_{liq}, \tag{20}$$

$$\langle C_{liq} \rangle_{V_{liq}} = \frac{1}{V_{liq}} \int_{V_{liq}} C_{liq} dV = \frac{1}{V_{liq}} C_{liq} V_{liq} = C_{liq}, \tag{21}$$

where C_{liq} is the concentration scalar in the liquid phase, V_{cell} the total computational cell volume and V_{liq} is the liquid-phase volume within the cell. The relationship between these two averages is given by $\langle C_{liq} \rangle_{V_{cell}} = f \langle C_{liq} \rangle_{V_{liq}}$ so that the liquid phase average can be expressed as $\langle C_{liq} \rangle_{V_{liq}} = \frac{\langle C_{liq} \rangle_{V_{cell}}}{f}$. This distinction becomes crucial in interface cells, where $0 < f < 1$, as the total volume average would dilute the concentration field and underestimate diffusion into the pure liquid cells. Therefore, for the diffusive part of Eq. (14), we apply the phase-averaged concentration $\langle C^{\Theta}_{salt} \rangle_{liq} = C^{\Theta}_{salt}/f$, which ensures that we predict the correct concentration gradient and thereby the correct diffusive flux from the interface cells to the pure liquid phase. After we diffuse the phase-averaged concentration field $\langle C^{\Theta}_{salt} \rangle_{liq}$, we convert the concentration scalar field back to a volume averaged field, to be consistent with the scalar concentration advection. This approach is also applied to the source term S^{Θ}_{mass}, as described in Tourbier et al. [44].

2.2. Initial, boundary and case conditions

To identify regions where supersaturation develops first, proper initial conditions are essential. The entire liquid film must initially satisfy the necessary condition $S^{\Theta}(t^{\Theta} = 0, \mathbf{x}^{\Theta}) < 1$, ensuring that it remains below the saturation limit. We prescribe an initial salt concentration field $C^{\Theta}(t^{\Theta} = 0, \mathbf{x}^{\Theta})^{init}_{salt}$ that meets this criterion. In industrial black liquor falling film applications, the typical temperature difference between the heat transfer wall and the gas–liquid interface is $\Delta T \approx 10$ K [45]. Accordingly, the initial wall temperature is set to $T_{wall}(t = 0, (0, y)) = 383$ K ($T^{\Theta} = 1$), while the interface is maintained at saturation temperature $T_{int}(t = 0, (\delta_N, y)) = T_{sat} = 373$ K ($T^{\Theta} = 0$). Under these conditions, the initial wall and interface saturation concentrations are $C^{sat}_{salt}(T(t = 0, (0, y))^{\Theta}) = 0.4375$ and $C^{sat}_{salt}(T(t = 0, (\delta_N, y))^{\Theta}) =$

0.4535, respectively. The wall temperature remains constant throughout the simulation, while the evaporation model, Eq. (15)–(16), ensures that for $R_{int} \to 0$, the interface temperature remains approximately at the saturation temperature due to evaporative cooling. Consequently, the saturation concentrations at the wall and interface remain constant throughout the simulation. It is important to note that, due to the evaporative cooling at the gas–liquid interface, the interfacial temperature does not fall below the initially prescribed saturation temperature. As a result, non-physical (spurious) condensation at the interface is not expected to occur in this region. The defined saturation concentrations are non-dimensionalized using a nearly constant liquid density $\rho_{liq} \approx 960\ \mathrm{kg/m^3}$ over a wide range of dry solid contents χ_s, Eq. (4). Selecting an initial uniform salt concentration of $C_{salt}^{init,\Theta}(t^\Theta = 0, \mathbf{x}^\Theta) = 0.43$ ensures that supersaturation is initially avoided in the film, with $S^{init,\Theta}(t^\Theta = 0, (0, y)^\Theta) \approx 0.98 < 1$ at the wall and $S^{init,\Theta}(t^\Theta = 0, (\delta_N, y)^\Theta) \approx 0.94 < 1$ at the interface, aligning well with the experimental observations from black liquor tests reported by Gourdon et al. [12].

The boundary condition framework follows mainly Hidman et al. [13], incorporating both inlet-outlet and periodic domain configurations. At the top of the computational domain, we impose the inlet volume fraction $f\left(0 \le x^\Theta \le \delta_N\right) = 1$ and $f\left(\delta_N < x^\Theta \le L_{Box}\right)$. The streamwise velocity profile at the inlet is prescribed according to the classical laminar solution derived by Nusselt [27], using the non-dimensional mean velocity $v_N = \left(Re^2/3\right)^{1/3}$

$$v^\Theta\left(0 \le x^\Theta \le \delta_N\right) = -\frac{3}{2} v_N \left[2\left(\frac{x^\Theta}{\delta_N}\right) - \left(\frac{x^\Theta}{\delta_N}\right)^2\right]\left(1 + \epsilon \sin(2\pi f^\Theta t^\Theta)\right), \tag{22}$$

$$v^\Theta\left(\delta_N < x^\Theta \le L_{Box}\right) = -\frac{3}{2} v_N, \tag{23}$$

where $\epsilon = 0.05$ is the perturbation amplitude and $f^\Theta = 0.0294$ ($f = 10$ Hz) is the non-dimensional perturbation frequency. The thermal boundary conditions are set as $T^\Theta = 1$ at the heated wall and $T^\Theta = 0$ at the inlet and far field, while an open outlet minimizes flow reflections [46]. The inlet-outlet setup is used for validation before transitioning to periodic boundary conditions in the streamwise direction, allowing for efficient computation of averaged heat fluxes, salt concentration fields, and supersaturation distributions over an industrially relevant evaporator pipe length. The main modification to the initial and boundary conditions in this study, compared to Hidman et al. [13], is the treatment of the salt concentration field. To ensure an initially undersaturated liquid film at $t^\Theta = 0$, C_{salt}^Θ is initialized as $C_{salt}^\Theta = 0.43$ for $0 \le x \le \delta_N$ and $C_{salt}^\Theta = 0$ for $\delta_N < x \le L_{Box}$. This enables a focused investigation of supersaturation onset and its spatial evolution under evaporative conditions.

In our simulations investigating liquid supersaturation dynamics, we systematically examine three distinct cases by varying the Reynolds number while maintaining a constant Kapitza number at $Ka \approx 500$ to ensure meaningful and representative comparisons. These cases correspond to Reynolds numbers $Re = 100$ (**C1**), $Re = 200$ (**C2**), and $Re = 400$ (**C3**). These Reynolds numbers reflect industrially relevant conditions for black-liquor applications at the specified Kapitza number. Among these, we define **C2** as our base scenario, as it closely corresponds to the conditions most frequently encountered in industrial applications [47]. The dry solid content χ_s, determined by the initial salt concentration, defines the thermophysical properties together with Eq. (3) - (6). The liquid Prandtl and Schmidt numbers remain constant at $Pr_l = 21$ and $Sc_l = 3216$, based on a mass diffusion coefficient of $D_{mass} = 10^{-9}\ \mathrm{m^2/s}$ [18]. The density and dynamic viscosity ratios are $\rho_l/\rho_g = 1014$ and $\mu_r = \mu_l/\mu_g = 156$, with gas-phase properties corresponding to air. All three simulations employ a periodic boundary with a non-dimensional size $L_{Box}/\delta_N = 200$, approximating the vertical separation of statistically steady solitary waves —nonlinear, capillary–gravity wave structures that retain their shape while propagating downstream and exhibit stable statistical properties over time.

2.3. Grid independence study

To ensure that our numerical simulations fully resolve the relevant hydro- and heat-transfer phenomena and satisfactorily reproduce those related to mass transfer, a systematic grid independence study is conducted. In essence, we want to convince the reader that our framework fully resolves advection in the film and at the same time provides a trustworthy reproduction of large-scale features of scalar mixing. Given the characteristic dimensionless numbers for the selected case — $Re = 100, Ka = 500, Pr_l = 21, Sc_l = 3216$ — the resolution requirements are predominantly governed by the smallest boundary layer thickness among the hydrodynamic-, thermal-, and mass-transfer boundary layers. While the thermal boundary layer is considerably thinner than the hydrodynamic one, the Schmidt number significantly exceeds the Prandtl number, resulting in an even thinner mass transfer boundary layer. Consequently, the steep concentration gradients within this layer dictate the required grid resolution. However, the exceptionally high Schmidt number ($Sc_l = 3216$) poses significant numerical challenges. In such regimes, the extremely low mass diffusivity leads to the formation of very thin concentration boundary layers, which are inherently difficult to fully resolve in numerical simulations. Inevitably, numerical diffusion becomes non-negligible and introduces an artificial enhancement to the effective diffusivity. As a result, diffusive transport is overestimated, leading to an artificially broadened concentration boundary layer, with the values of local supersaturation peaks potentially underestimated. We do not find this as a problem since similar discussions, with the differences also in mind, are found in, for example, the general implicit Large Eddy Simulation (LES) community [48] or studies that use LES to look at high Sc number mass transfer at gas–liquid interfaces [49]. In the former case, acceptable large-scale turbulent statistics are reported (even if the velocity field is under resolved, which is not the case in our work), whereas the latter study postulates that "the mass transfer at a gas–liquid interface is governed by the large-scale motion" (otherwise, LES would be by definition useless to provide accurate prediction of the mass-transfer rate). Although the mentioned numerical artifact implies that the small-scale structures of the concentration field may be smeared, we argue that the large-scale features remain consistent and reliable due to the fully resolved hydrodynamics. In other words, despite the limitations in addressing the small-scale diffusional mixing, we claim that our simulation framework is a reliable tool for capturing the dominant transport dynamics and assessing scalar mixing behavior at the macroscopic level. To prove our point, we have carried out the simulations with grid resolutions ranging from $11\Delta/\delta_N$ to $168\Delta/\delta_N$, systematically refining the grid to determine a trustworthy degree of resolution for our relevant flow and transport phenomena.

In Fig. 3**(a)**, we analyze the gas–liquid interface profiles along the normalized streamwise direction and observe negligible differences between the results at $21\Delta/\delta_N$, $42\Delta/\delta_N$ and $84\Delta/\delta_N$. This indicates that a grid resolution of $21\Delta/\delta_N$ is sufficient to accurately capture the hydrodynamics. Similarly, in Fig. 3 **(b)**, we examine the average non-dimensional temperature profiles in the wall-normal direction under statistically steady conditions. In the present context, the term *statistically steady* refers to a flow regime in which time-averaged quantities - such as velocity, temperature, and other scalar fields - exhibit no systematic variation in the streamwise direction. That is, after sufficient temporal averaging, the mean profiles become invariant along the flow direction, indicating the absence of streamwise evolution [14]. $T^\Theta = 1$ corresponds to the temperature at the heat transfer wall, and $T^\Theta = 0$ represents the saturation temperature, according to Eq. (9). The results show that, for the selected Prandtl number, a grid resolution of $21\Delta/\delta_N$ is also sufficient to resolve the spatial variation of the thermal phenomena. Fig. 3**(c)** presents the liquid-phase streamwise averaged, non-dimensional salt concentration field along the normalized wall-normal direction for various grid resolutions. Unlike the hydrodynamic and thermal fields, which are sufficiently resolved with

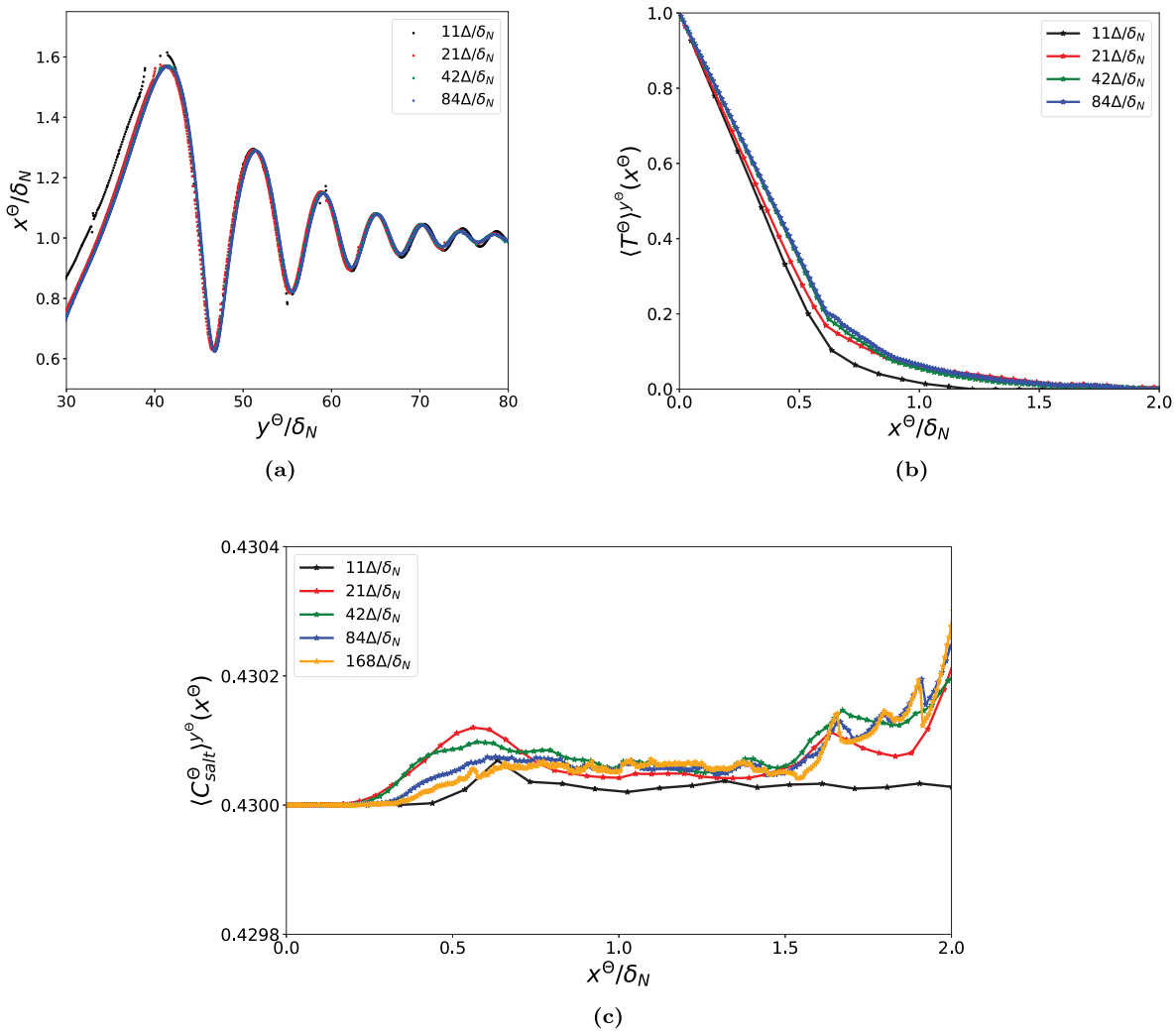

Fig. 3. Grid independence study for hydrodynamics, heat- and mass transfer ($Re = 100, Ka = 500, Pr_l = 21, Sc_l = 3216$) with different grid resolutions per film thickness. (*a*) Gas–liquid interface profile development in streamwise direction. (*b*) Average non-dimensional temperature profiles in wall-normal direction computed at statistically steady conditions. (*c*) Liquid-phase streamwise averaged (Eq. (27)), non-dimensional salt concentration profiles in wall-normal direction.

$21\Delta/\delta_N$, the mass transfer field exhibits a much stronger sensitivity to grid refinement due to the low mass diffusivity. Coarse resolutions ($11\Delta/\delta_N, 21\Delta/\delta_N$) fail to capture the concentration field accurately, and even $42\Delta/\delta_N$ shows noticeable deviations. At $84\Delta/\delta_N$, the results agree fairly well with those at $168\Delta/\delta_N$, which is the finest grid resolution in our studies. Since further refinement yields only marginal improvements, $84\Delta/\delta_N$ is identified as a satisfactory compromise, ensuring that hydrodynamics and heat transfer are fully resolved and a satisfactory resolution of mass transfer effects in agreement with the discussion presented in the beginning of this section.

2.4. Validation

To demonstrate the reliability of our numerical framework, we validate our hydrodynamic, heat transfer, and mass transfer predictions against established numerical, experimental, and analytical results. Fig. 4 presents the comprehensive validation results, where **(a)** compares the simulated free surface hydrodynamic profile with the numerical findings of Åkesjö et al. [22] and Doro and Aidun [21], **(b)** evaluates the predicted heat transfer rates against well-established experimental correlations, and **(c)** examines the salt concentration profiles in comparison to an analytical solution for a flat, evaporating falling film.

For the hydrodynamic validation, the free surface profile is evaluated at a constant liquid volume fraction of 0.5 and a specific time instant. Both axes are normalized using the non-dimensional Nusselt film thickness δ_N. The working fluid is water, with $Re = 69$, $Ka = 3394$, and a perturbation frequency $f = 70$ Hz. The results from our numerical framework demonstrate strong agreement with previous studies, effectively capturing the hydrodynamic behavior of a falling liquid film, as shown in Fig. 4 **(a)**.

The heat transfer validation is performed by assessing the predicted heat transfer rates of our numerical framework. The Nusselt number $Nu = \frac{\bar{q}_{evap}}{k_l(T_{wall}-T_{sat})}\left(\nu_l^2/g\right)^{1/3}$ [38] provides a dimensionless measure of the ratio between convective and conductive heat transfer and is compared with the experimental correlations of Numrich [50] and Gourdon et al. [16], which are valid for Prandtl numbers up to 52 and 800, respectively and mainly used to predict heat transfer rates in falling film applications

$$Nu_{Numrich} = \sqrt{(0.9Re^{-1/3})^2 + (0.0055Re^{0.44}Pr^{0.4})^2}, \tag{24}$$

$$Nu_{Gourdon} = \sqrt{(0.9Re^{-1/3})^2 + (0.011Re^{0.2}Pr^{0.65})^2}. \tag{25}$$

Using a liquid Prandtl number of $Pr_l = 21$ and varying Re between 100 and 400, we compute the evaporative heat-flux, Eq. (15), under statistically steady conditions, and validate the Nusselt number. Fig. 4**(b)** shows that the predicted Nusselt numbers agree closely with the correlation proposed by Gourdon et al. [16] and also lie within the

reported error margins of both experimental datasets. This agreement supports the accuracy of the framework in capturing the heat transfer behavior of the falling film.

To validate the numerical predictions of the salt concentration field, C^{Θ}_{salt}, we compare our results against the analytical solution for transient diffusion in a flat film with constant evaporative flux at the gas–liquid interface, as derived by Crank [51]

$$C - C_0 = \frac{\dot{m}''_{theo} h_N}{D}\left(\frac{Dt}{h_N^2} + \frac{3x^2 - h_N^2}{6h_N^2} - \frac{2}{\pi^2}\left[\sum_{n=1}^{\infty}\frac{(-1)^n}{n^2}\exp\left(\frac{-Dn^2\pi^2 t}{h_N^2}\right)\cos\left(\frac{n\pi x}{h_N}\right)\right]\right) \tag{26}$$

where $C = C_{salt}(t, x)$ denotes the transient concentration profile, $C_0 = C_{salt,0}$ the initial uniform concentration, and x the wall-normal coordinate. The theoretical evaporative mass flux $\dot{m}''_{theo}$ is determined from the energy balance between the purely conductive heat flux through the liquid film and the latent heat of vaporization at the gas–liquid interface, expressed as $\dot{q}''_{wall} = \dot{q}''_{evap,theo}$, where $\dot{q}''_{wall} = k_l \frac{T_{wall} - T_{sat}}{h_N}$ and $\dot{q}''_{evap,theo} = \dot{m}''_{theo} h_{fg}$. As the film thickness h_N remains constant, the evaporative mass flux $\dot{m}''_{theo}$ is time-invariant. The analytical concentration profile is incorporated into the non-dimensional framework defined in Eq. (9) for direct comparison with numerical results. The validation is carried out over a characteristic wave pass frequency of $f_{wave} = 10$ Hz (corresponding to $t_{wave} = 0.1$ s), describing the time between two consecutive waves, as experimentally observed by Åkesjö et al. [22] under similar operating conditions, but also confirmed through DNS studies in this work.

The results of this validation are presented in Fig. 4**(c)**, where the numerical solutions for different grid resolutions are compared against the analytical solution at $t = 0.1$ s $= t_{wave}$. The results highlight the already discussed challenges encountered when attempting to fully resolve high Schmidt number transport at such small timescales. While finer grid resolutions (e.g. $672\Delta/\delta_N$) yield improved agreement with the analytical solution, the computational cost becomes prohibitively high. A resolution of $84\Delta/\delta_N$ with around 5 grid points in the mass transfer boundary layer provides a reasonable compromise, showing fairly good agreement with both the analytical solution and the highest resolution numerical results, while significantly improving accuracy compared to the coarser grid. Our confidence that we reliably, and at acceptable computational costs, reproduce large-scale features of scalar mixing in the film is further supported by the grid independence study discussed in Section 2.3.

3. Results and discussion

In this section we present the simulation results on the dynamics of liquid supersaturation in evaporating vertical falling films over smooth heat transfer surfaces for a periodic domain. We begin with a qualitative overview of the key scalar fields for our base case, providing insight into the fundamental mechanisms governing supersaturation. This is followed by a quantitative analysis of the temporally and spatially averaged scalar properties, highlighting their contributions to our general hypothesis on liquid supersaturation. Finally, we examine the influence of the Reynolds number (reflecting the film wetting rate) on the supersaturation dynamics, comparing and discussing its impact on film behavior.

3.1. Qualitative analysis of scalar fields governing supersaturation

Liquid supersaturation dynamics in evaporating falling films are governed by the coupled effects of heat and mass transfer, interfacial evaporation and temperature-dependent solubility. As discussed previously, the spatiotemporal evolution of supersaturation is driven by two principal mechanisms: (i) interfacial evaporation, which increases the local salt concentration near the gas–liquid interface through solvent removal, and (ii) inverse solubility, which promotes supersaturation near the heated wall due to reduced solubility at elevated temperatures. To qualitatively evaluate these mechanisms, we examine the spatial distribution of key scalar fields — temperature, saturation concentration, salt concentration, and supersaturation — based on scalar-field visualizations. By examining these fields, we aim to identify regions within the film with a high local supersaturation and to study the interplay of the two driving mechanisms.

Fig. 5 presents zoomed-in snapshots of scalar fields for the base case **C2** with $Re = 200$, illustrating the interrelated distributions of temperature, saturation concentration, salt concentration, and supersaturation within the falling film. In subfigure (**a**), the non-dimensional temperature field T^{Θ} shows a distinct thermal boundary layer adjacent to the heated wall, with $T^{\Theta} = 1$ at the wall and a gradual decrease toward the gas–liquid interface, where $T^{\Theta} \approx 0$, driven by evaporative cooling. The interface, indicated by the white contour, highlights the wave structure composed of a dominant solitary wave and smaller capillary undulations. Local thermal protrusions from the wall into the bulk suggest internal convective transport structures. Subfigure (**b**) displays the saturation concentration field $(C^{sat}_{salt})^{\Theta}$, which inversely follows the temperature distribution due to the inverse solubility of the salt. Lower values appear near the heated wall, where the temperature is high, while higher saturation concentrations are seen near the cooler interface, reflecting the thermal gradient across the film. In subfigure (**c**), the salt concentration C^{Θ}_{salt} is relatively uniform near the wall, while localized variations and banded structures within the wave point to convective mixing and redistribution of the salt concentration field. Additionally, elevated concentrations are observed in the vicinity of the gas–liquid interface, associated with interfacial evaporation. Subfigure (**d**) presents the supersaturation field S^{Θ}, which resembles the salt concentration field. The values remain below unity near the heated wall but increase toward the interface. Pronounced supersaturation regions emerge beneath the wave crest and near the interface, reflecting local solute enrichment in conjunction with a reduced solubility. The enrichment of S^{Θ} in the interfacial region indicates that the onset of supersaturation is strongly associated with evaporative solvent removal at the film interface.

We reiterate here that, in Basilisk, a computational domain is defined as a square with its origin located at the bottom-left corner. When generating visualizations or snapshots in ParaView, the default coordinate system is typically positioned outside the physical domain, which can hinder interpretability, especially in zoomed-in views. To improve clarity and aid the reader's spatial understanding, we chose to reposition the coordinate system within the computational domain. Furthermore, we carefully aligned the coordinate axes in the visualizations to reflect the principal flow direction in the zoomed-in regions, thereby enhancing the physical interpretability of the depicted flow structures.

3.2. Segmentation and averaging framework for supersaturation analysis

To facilitate the subsequent quantitative analysis of governing liquid supersaturation dynamics in evaporating vertical falling films, we first define the spatial segmentation of the system. The studied system comprises an industrial-scale evaporator pipe with a total length of 10 m. To capture the spatial evolution of key governing fields along the film flow, we subdivide the evaporator into three distinct sections: **Top** (0 m → 1 m), Middle (4 m → 5 m) and **Bottom** (9 m → 10 m) (see Fig. 6). This segmentation enables a structured analysis of the onset of supersaturation and its spatiotemporal progression, allowing us to assess whether supersaturation is predominantly driven by interfacial evaporation or inverse solubility effects.

To ensure a statistically robust characterization of the governing fields, we employ a two-step averaging procedure — temporal averaging followed by spatial averaging — which minimizes transient

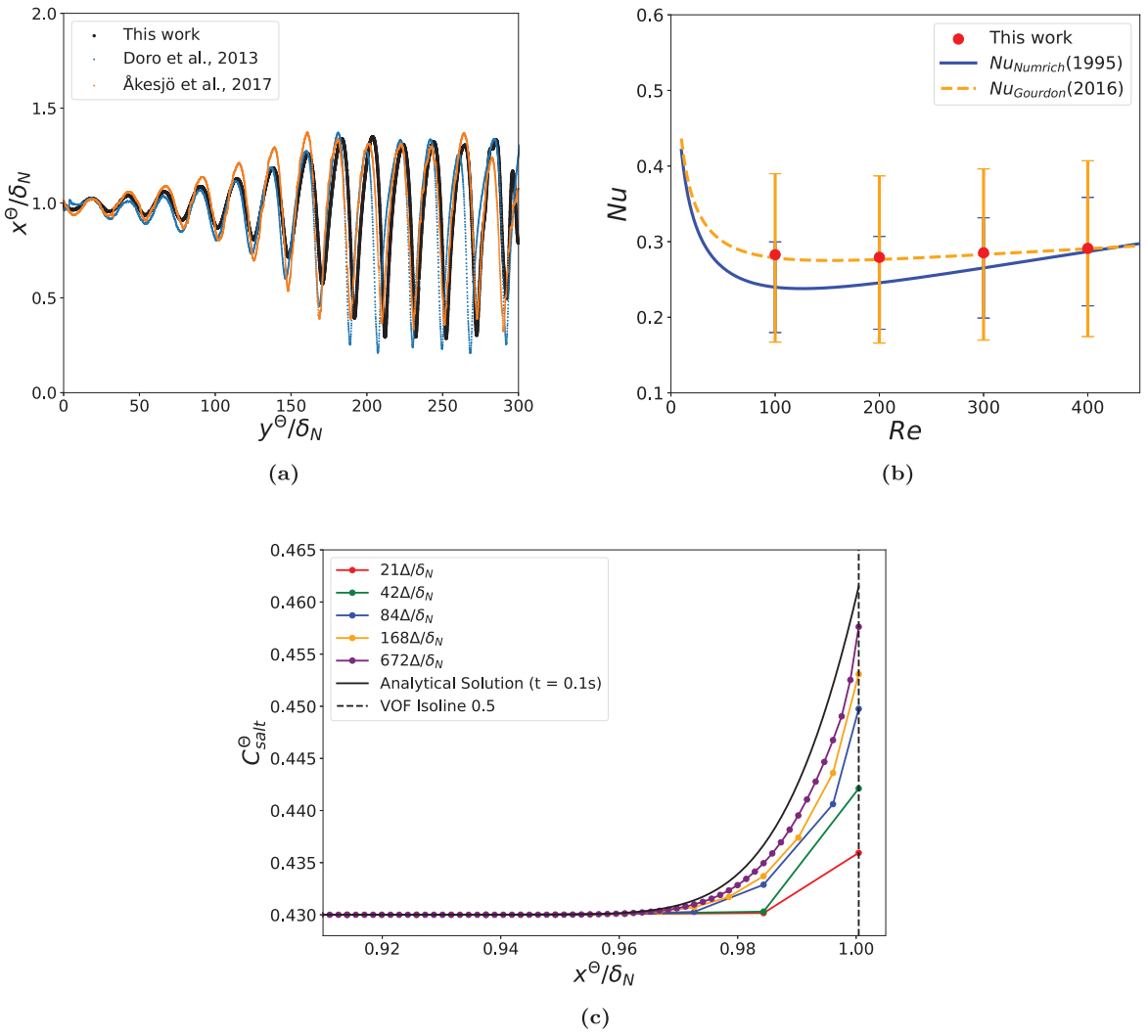

Fig. 4. Validation of hydrodynamics, heat transfer, and mass transfer through comparison with established numerical, experimental, and analytical results. **(a)** Gas–liquid interface profiles for $Re = 69$, $Ka = 3394$, and $f = 70\ Hz$, with normalized axes. **(b)** Nusselt number Nu as a function of Reynolds number Re for evaporative falling film with $Ka = 1000$, $Pr_l = 21$, and Re varying from 100 to 400. **(c)** Comparison of numerical and analytical salt concentration profiles, C^Θ_{salt}, for a flat, evaporating film characterized by $Re = 200$, $Ka = 500$, $Pr_l = 21$, and $Sc_l = 3216$ at a physically relevant time scale $t_{wave} = 0.1\ s$, describing the time between two consecutive waves that disturb the mass transfer boundary layer. The VOF Isoline 0.5 indicates the gas–liquid interface.

fluctuations while preserving the essential dynamics of supersaturation development. First, temporal averaging is applied to a general scalar field Ψ^Θ (representing temperature, salt concentration, or supersaturation), where accumulation is restricted to the liquid phase by considering only grid points with a volume fraction that satisfies $f > 10^{-12}$. The summation over all time steps is then normalized by the total number of valid liquid-phase contributions, yielding the temporally averaged field. The temporally averaged field is subsequently averaged along the streamwise direction y^Θ, resulting in a final wall-normal profile $\Psi^\Theta(x^\Theta)$ that represents the mean distribution of the scalar quantity across the film. At this point, we emphasize that the two-step averaging procedure is not applied over the entire length of the evaporator tube. Instead, the domain is subdivided into the three highlighted representative sections - **Top**, **Middle**, and **Bottom** - each spanning approximately 1 m in streamwise length. Averaging is performed independently within each section. This sectional approach enables us to capture and analyze variations in supersaturation dynamics along the evaporator length. It also provides evidence that the propensity for scaling in falling film evaporators is not uniform but is more likely to occur in specific regions of the tube, depending on local flow and transport conditions.

A fundamental requirement for accurately capturing the full evolution of the falling film in our simulations is the determination of an appropriate simulation end time. To achieve this, we estimate the characteristic time scale for the fluid to traverse the entire 10 m pipe length. The flow through time, $t_{flow,through}$, is defined as $t_{flow,through} = h_{pipe}/u_{film}$ where h_{pipe} represents the total length of the pipe, and u_{film} is the characteristic velocity of the falling film. To approximate u_{film}, we compute the liquid-phase averaged streamwise velocity, which provides a representative velocity scale to estimate $t_{flow,through}$. The liquid-phase averaged streamwise velocity is defined as

$$\langle u_l^\Theta \rangle \left(y^\Theta\right) = \frac{1}{\int_{\Omega^\Theta} f\, d\Omega^\Theta} \int_{\Omega^\Theta} u_l^\Theta \left(y^\Theta\right) f\, d\Omega^\Theta \tag{27}$$

where Ω^Θ describes the entire domain. Since the characteristic velocity of the film is strongly influenced by Re, the flow-through time inherently depends on the flow regime. For our base case, **C2**, we estimate $t_{flow,thorugh} \approx 11$ s. By using this velocity to determine $t_{flow,through}$, we establish a well-defined simulation end time that fully encompasses the film's development along the entire pipe length.

3.3. Quantitative analysis of scalar fields governing supersaturation

In Section 3.1, we qualitatively analyzed the governing scalar fields defining supersaturation and described their observed behaviors. Here,

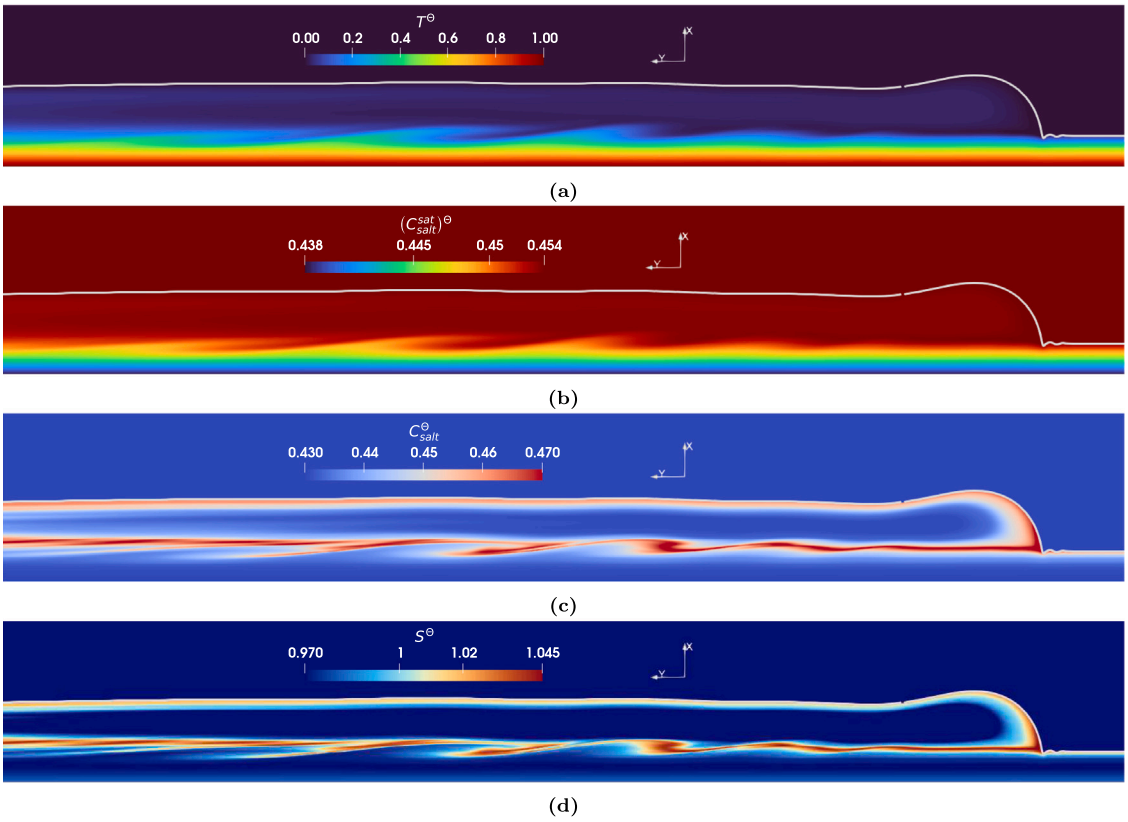

Fig. 5. Scalar field distributions for the base case **C2** ($Re = 200$). (a) Non-dimensional temperature field T^Θ; (b) non-dimensional saturation concentration field $(C^{sat}_{salt})^\Theta$; (c) non-dimensional salt concentration field C^Θ_{salt}; (d) non-dimensional supersaturation field S^Θ. The streamwise flow and gravitational acceleration act in the negative y-direction, while x denotes the wall-normal coordinate. For visualization purposes, the film domain has been rotated counterclockwise. In each subfigure, the white contour line represents the gas–liquid interface.

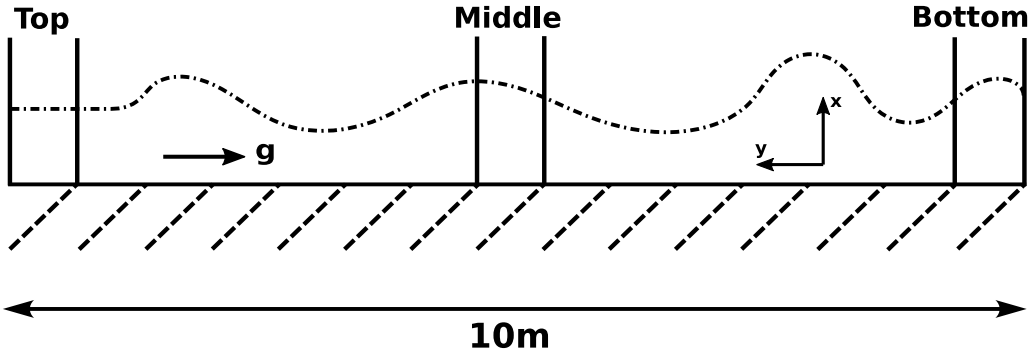

Fig. 6. Schematic representation of the evaporator pipe, divided into three sections: Top, Middle, and Bottom, for spatially resolved analysis. For visualization purposes, the figure has been shifted such that gravity appears to act horizontally. The dashed line represents the gas–liquid interface. The total pipe length is 10 m, corresponding to an industrial-scale evaporator.

we extend our investigation by performing a detailed quantitative analysis, with the aim of characterizing the spatial and temporal evolution of supersaturation and the associated scalar fields. Our quantitative examinations are focused on the base case, **C2**, allowing direct comparisons with the qualitative insights presented earlier in Section 3.1. As previously outlined in Section 3.2, the pipe domain is systematically partitioned into three distinct regions — Top (0 m → 1 m), Middle (4 m → 5 m), and Bottom (9 m → 10 m) — to methodically explore and quantify the dynamics and interplay of supersaturation and its underlying scalar fields.

Fig. 7 presents the governing scalar fields relevant to supersaturation, showing liquid-phase streamwise and temporally averaged distributions. Specifically, the y-axis in each subfigure represents the averaged non-dimensional quantities, including the temperature T^Θ, the salt concentration C^Θ_{salt}, and the supersaturation S^Θ itself. The x-axis represents the wall-normal distance, normalized by the non-dimensional film thickness δ_N, where $x^\Theta/\delta_N = 0$ corresponds to the heated wall, and the value of 1 to the initial film thickness and therefore the gas–liquid interface. During the streamwise flow of the film, roll waves develop, which leads to a change in the local film thickness. The wave crest exceeds the initial film thickness and reaches its maximum at approximately $x^\Theta/\delta_N \approx 1.8$, representing also the maximum limit of the x-axis.

The Top region, corresponding to the initial streamwise segment near the film inlet (0 m → 1 m), represents the early stage of hydrodynamic development, characterized by a relatively thin, undisturbed

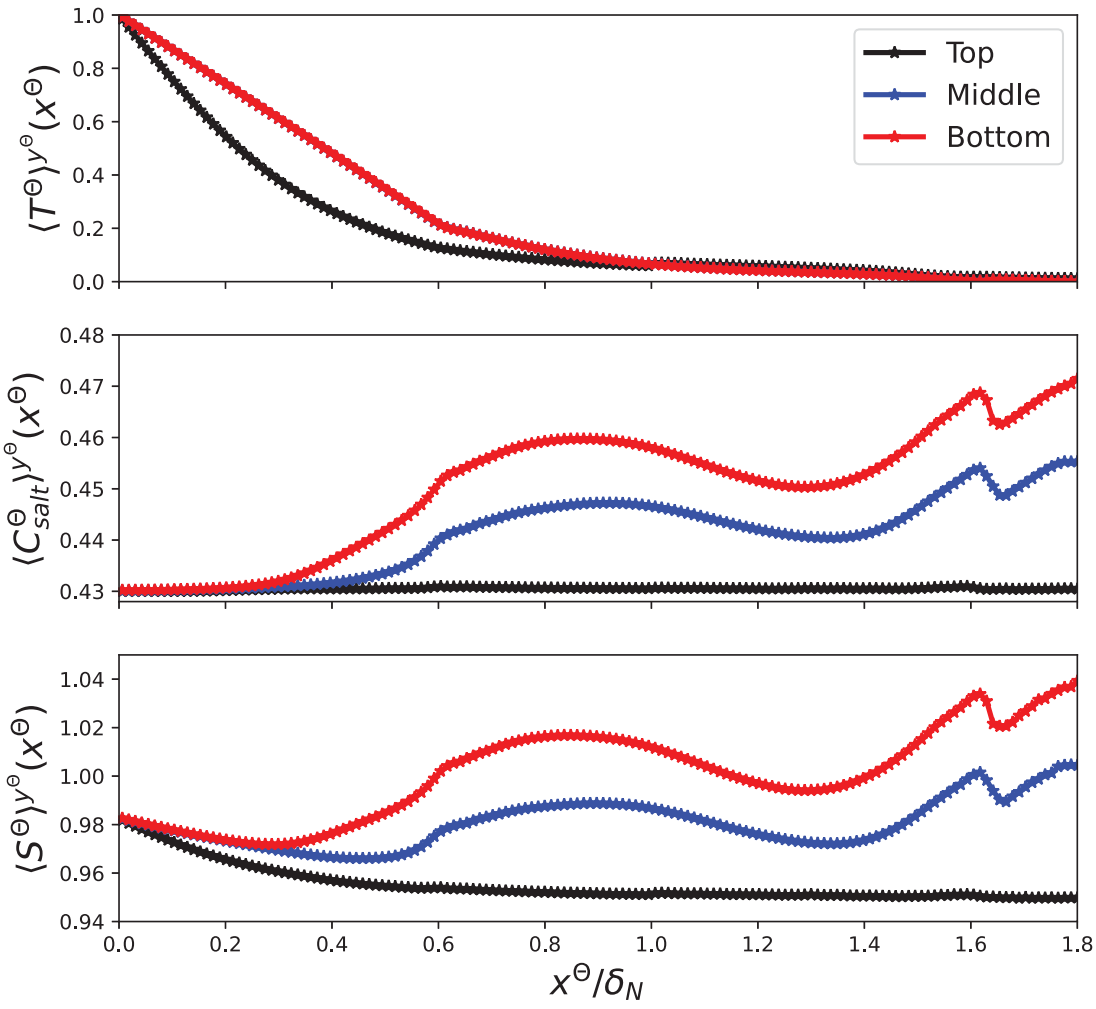

Fig. 7. Temporally and streamwise-averaged distributions of the governing scalar fields in the liquid phase for the base case **C2**. Each subfigure presents the wall-normal profiles of non-dimensional temperature T^Θ, salt concentration C^Θ_{salt}, and supersaturation S^Θ, respectively. The y-axis in each plot represents the non-dimensional scalar quantity, while the x-axis denotes the non-dimensional wall-normal coordinate, normalized by the non-dimensional Nusselt film thickness δ_N, with $x^\Theta/\delta_N = 0$ corresponding to the heated wall and $x^\Theta/\delta_N = 1$ to the initial gas–liquid interface. The extended domain up to $x^\Theta/\delta_N \approx 1.8$ accounts for the local film thickening due to wave development. Results are shown for the Top, Middle, and Bottom sections of the evaporator, Fig. 6, enabling direct comparison of scalar field evolution along the film height.

liquid film whose gas–liquid interface closely aligns with the initial film thickness. Within this region, the scalar fields largely retain initial conditions, as the fluid dynamic and scalar transport mechanisms have not yet fully evolved. The non-dimensional temperature field T^Θ exhibits a distinct nonlinear distribution near the heated wall, beginning at unity at the wall (where $x^\Theta/\delta_N = 0$) and sharply decreasing to approximately 0.1 at $x^\Theta/\delta_N \approx 0.8$. This rapid decrease over a short wall-normal distance reflects the formation of a thermal boundary layer dominated by conductive heat transfer from the heated wall, characteristic of the upstream region of laminar falling films. As the boundary layer develops further downstream, evaporative cooling at the gas–liquid interface becomes increasingly significant [47]. Beyond $x^\Theta/\delta_N = 0.8$, the temperature distribution transitions toward a nearly linear profile, indicative of a quasi-steady thermal regime establishing as evaporative interface cooling regulates the temperature, leading to near thermal saturation condition around $x^\Theta/\delta_N \approx 1$. Simultaneously, the non-dimensional salt concentration field C^Θ_{salt} maintains a largely uniform profile, starting with a value of 0.43 adjacent to the heated wall, and experiencing negligible variations across the film thickness. The uniformity of this scalar field quantitatively confirms the not yet fully developed temperature distribution and therefore the minimal evaporative heat flux at the gas–liquid interface, leading to negligible wall-normal concentration gradients. Consequently, solute transport within the top region is primarily governed by streamwise advective processes. In direct correlation with the temperature and salt concentration fields, the supersaturation field S^Θ begins near 0.98 at the wall and gradually declines to about 0.95 at around $x^\Theta/\delta_N \approx 0.8$, the same wall-normal distance as that of the thermal boundary layer development. This slight but clear decrease is quantitatively consistent with the temperature-dependent solubility characteristic of the inverse-soluble salt, as defined in Eq. (1). Here, close to the heated wall, the increased temperature leads to a decreased solubility limit (C^{sat}_{salt}), consequently elevating the supersaturation S^Θ. In contrast, near the gas–liquid interface, lower temperatures enhance the solubility, resulting in reduced supersaturation values. This inverse solubility mechanism clearly dominates supersaturation dynamics in the Top region, given the minimal evaporative enrichment and the predominance of advective over diffusive transport.

In the Middle region, corresponding to the intermediate section of the evaporator pipe, the temperature field T^Θ transitions to a distinctly linear distribution, characteristic of a fully developed laminar thermal boundary layer. Near the heated wall, the temperature remains elevated around 1 and gradually decreases to approaching saturation conditions in the vicinity of the gas–liquid interface at approximately

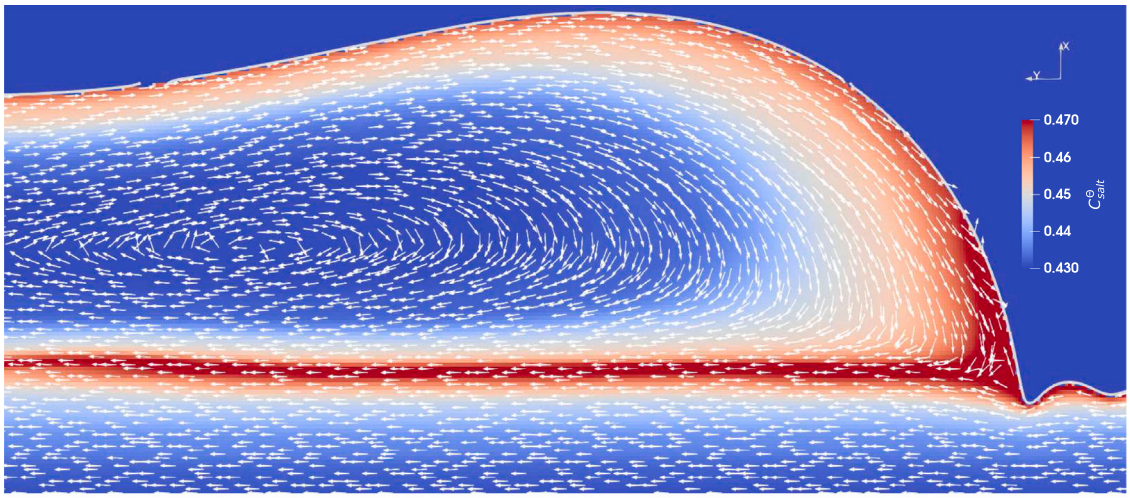

Fig. 8. Non-dimensional salt concentration field C^{Θ}_{salt} for the base case **C2**, focusing on the roll wave front and the preceding capillary waves. The overlaid white arrows indicate the velocity field within the liquid film, in a reference frame moving with the wave front. Clearly visible is the internal recirculation in the roll wave, associated with the solute trapping and redistribution. The white line represents the gas–liquid interface.

$x^{\Theta}/\delta_N \approx 1.6$. Compared to the Top region, the Middle region exhibits more stable thermal gradients, indicating the development of a steady thermal profile governed by consistent evaporative heat removal. This is consistent with the qualitative visualizations, which show uniform thermal stratification, Fig. 5 (**a**). The salt concentration field C^{Θ}_{salt} in the Middle region reveals a non-monotonic profile. Here, $C^{\Theta}_{salt} \approx 0.43$ at $0 \leq x^{\Theta}/\delta_N \approx 0.4$ but, further out from the wall, the concentration increases and reaches a local maximum of approximately 0.45 at $x^{\Theta}/\delta_N \approx 0.9$. This localized enrichment originates from interfacial evaporation and flow separation in the capillary region, where internal recirculation in the roll wave transports the high concentration liquid from the interface into the wave interior. As shown in Fig. 8, the resulting clockwise vortex becomes embedded within the reference frame of the wave and is transported downstream along the film. At the front slope of the wave, advection in the x-direction is clearly observed (the upward pointing velocity vectors), where the fluid from the lower boundary layer is lifted vertically (in the x-direction) due to local flow acceleration. This upward transport carries salt-rich fluid toward the mid-height and upper regions of the film, significantly contributing to the observed concentration peak through vertical redistribution. The reversal of the flow reduces streamwise transport, while relatively weak wall-normal diffusion limits the scalar redistribution and mixing. As a result, salt accumulates within the film mid height (see Fig. 5 (**c**) and Fig. 8), producing the observed local maximum in C^{Θ}_{salt} at a wall-normal distance of $x^{\Theta}/\delta_N \approx 0.9$, compare Fig. 7. Following this local enrichment zone in the quantitative results, the concentration decreases to approximately 0.44 at $x^{\Theta}/\delta_N \approx 1.3$, corresponding to the transition to the wave crest and its recirculation and backflow property. However, closer to the gas–liquid interface, C^{Θ}_{salt} increases again, reaching a global maximum of approximately 0.455 near $x^{\Theta}/\delta_N \approx 1.6$. This secondary increase is primarily attributed to intensified interfacial evaporation, which selectively removes the solvent and enriches the solute near the interface at the wave crest. This dual-peak behavior underscores how internal recirculation governs solute accumulation within the wave body, while interfacial evaporation drives enrichment near the interface. Together, these mechanisms shape the salt concentration field and highlight the intricate coupling between the internal film hydrodynamics and interfacial mass transfer.

The supersaturation field S^{Θ} in the Middle region closely follows the trends in C^{Θ}_{salt}, as it is directly governed by the ratio $S^{\Theta} = C^{\Theta}_{salt}/\left(C^{sat}_{salt}\right)^{\Theta}$. Therefore, the physical interpretation of the salt concentration field is directly applicable to the supersaturation distribution in the film. However, it is important to note that near the heated wall, the elevated values of S^{Θ} are not due to local salt enrichment but rather result from the inverse solubility behavior — where higher temperature reduces the solubility limit $\left(C^{sat}_{salt}\right)^{\Theta}$, thereby increasing supersaturation. This effect, evident in both snapshots and quantitative results, highlights the distinct thermodynamic contribution to supersaturation in the regions lacking significant salt accumulation.

In the Bottom region, which represents the final stage of film evolution near the pipe outlet, the temperature profile remains unchanged relative to the Middle region, indicating that the thermal boundary layer is fully developed and no further temperature evolution occurs. Both the salt concentration and supersaturation fields follow the qualitative structure observed in the Middle region, but with a progressive increase in magnitude. This enhancement results from the continued action of interfacial evaporation, which removes the solvent and leads to cumulative solute enrichment as the film descends. Notably, the profiles for C^{Θ}_{salt} and S^{Θ} become broader in the Bottom region compared to those in the Middle region, reflecting the growing influence of mixing and diffusion over longer residence times. However, because of the inherently slow nature of solute diffusion in the liquid, the region near the heated wall remains relatively unaffected by solute accumulation. Consequently, the fluid in the wall-adjacent region remains undersaturated, and the supersaturation is still predominantly governed by the inverse solubility effect.

Additionally, in Fig. 9, we present a zoomed-in view of the salt concentration field C^{Θ}_{salt} in the capillary region immediately in front of the solitary wave, corresponding to the detailed region highlighted in Fig. 8. Fig. 9 shows the non-dimensional, liquid phase averaged salt concentration field overlaid with the computational grid and the gas–liquid interface, depicted by the thick white line. This visualization qualitatively confirms that the strong interfacial curvature characteristic of capillary wave dynamics is spatially well resolved. The clear diffusion of the solute from the interface cells into the liquid bulk aligns with the issues related to the small-scale interfacial mass transfer behavior previously discussed in Section 2.3 and validated in Section 2.4 and Fig. 4, thereby reinforcing confidence in the numerical framework's ability to satisfactorily capture transport phenomena in wavy falling films. Moreover, the chosen grid resolution has been verified to reasonably well approximate the steep concentration gradients within the mass transfer boundary layer, yielding a fair agreement with the corresponding analytical solution (Fig. 4*c*) and confirming the adequacy of the spatial discretization.

In summary, the quantitative analysis of the governing scalar fields—temperature, salt concentration, and supersaturation—across the Top,

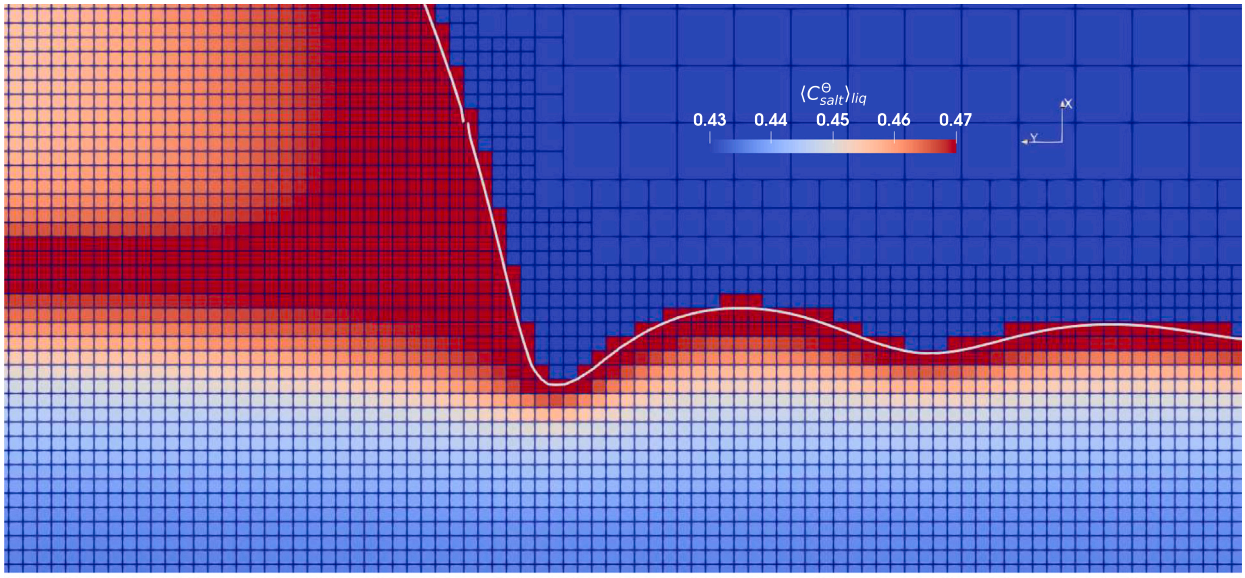

Fig. 9. Zoomed view of the non-dimensional salt concentration field, liquid phase averaged $\langle C^{\Theta}_{salt}\rangle_{liq}$ (compare Eq. (21)) in the capillary region upstream of the solitary wave for case **C2** ($Re = 200$), extracted from Fig. 8. The overlaid computational grid and the gas–liquid interface (white line) highlight the fine spatial resolution of interfacial curvature variations and the presence of a steep mass transfer boundary layer near the interface.

Middle, and Bottom regions of the film reveals a clear progression of heat and mass transfer processes throughout the film. While the temperature field rapidly develops into a quasi-steady linear profile due to evaporative cooling, the salt concentration and supersaturation fields exhibit spatially evolving structures shaped by the interplay of advection, diffusion, interfacial evaporation, and localized hydrodynamic phenomena such as internal recirculation. Supersaturation, in particular, emerges as a result of both solute enrichment and the thermodynamic effect of inverse solubility, with its distribution reflecting the coupled dynamics of concentration and temperature fields. Although the onset and intensification of supersaturation are clearly observed and quantified, the precise spatial conditions for its initial emergence remain to be clarified.

3.4. Spatial onset and development of supersaturation

Having analyzed in detail the temporal and spatial evolution of supersaturation and its governing scalar fields, we now focus on the appearance of supersaturation within the falling film and aim to identify dominant driving mechanisms. Specifically, we investigate whether interfacial evaporation or inverse solubility — or a combination of both — is primarily responsible for initiating supersaturation in the liquid phase. Fig. 10 presents the non-dimensional supersaturation field S^{Θ}, averaged temporally and streamwise over successive time intervals in the liquid phase. The dashed line indicates the saturation limit, and the necessary condition for supersaturation is met when $S^{\Theta} > 1$. The different time intervals correspond to downstream regions of the evaporator pipe, see Fig. 6 and Section 3.2, thus capturing the streamwise evolution of supersaturation. In the initial stages (0 s → 1 s, 2 s → 3 s), the film remains fully undersaturated, with maximum values of $S^{\Theta} \leq 0.98$ in the vicinity of the heated wall, reflecting the inverse solubility effect in this region of the film. As the film evolves, supersaturation gradually develops, and the threshold $S^{\Theta} > 1$ is first exceeded during the 6 s → 7 s interval. The onset is initially observed in the vicinity of the gas–liquid interface, highlighting interfacial evaporation as the primary driving force for the initial emergence of supersaturation. The removal of solvent at the interface increases the local solute concentration, while the solubility remains nearly constant, due to evaporative cooling that keeps the interface region at the saturation temperature and thereby satisfies the supersaturation criterion $S^{\Theta} = C^{\Theta}_{salt}/(C^{sat}_{salt})^{\Theta} > 1$. At later times (8 s → 9 s), hydrodynamic mechanisms — particularly internal recirculation within wave structures — redistribute the solute-rich fluid from the interface to the interior of the film. This transport leads to the development of secondary supersaturated regions at mid-film height, where salt becomes trapped due to streamwise advection and limited wall-normal diffusion. Furthermore, with increasing the flow time, it can be expected that advection and diffusion gradually transport the enriched fluid toward the heated wall, as can be interpreted by Fig. 7. In this region, the influence of the inverse solubility becomes increasingly significant: as C^{Θ}_{salt} increases and $(C^{sat}_{salt})^{\Theta}$ decreases due to elevated wall temperatures, their combined effect leads to a local rise in S^{Θ}. This thermodynamically induced increase in supersaturation illustrates a secondary mechanism that may become dominant near the wall under a long residence time.

In summary, the results demonstrate that while both interfacial evaporation and inverse solubility contribute to the evolution of supersaturation, only interfacial evaporation is responsible for the initial onset. Hydrodynamically induced transport subsequently redistributes these supersaturated regions, and prolonged exposure to thermal and solutes' gradients eventually enables the inverse solubility effects to further elevate S^{Θ}, particularly near the heated wall. This sequential interplay clearly delineates the distinct roles of thermodynamic and hydrodynamic mechanisms in the spatio-temporal development of supersaturation in falling films.

3.5. Influence of the Reynolds number (wetting rate) on supersaturation dynamics

As introduced in Section 2.2, three Reynolds number cases are simulated — $Re = 100$ (**C1**), $Re = 200$(**C2**), $Re = 400$ (**C3**) — with **C2** serving as the base case. Fig. 11 shows the non-dimensional supersaturation field S^{Θ} for the lower Reynolds number case $Re = 100$ (**C1**). The structure of the supersaturation field is qualitatively similar to that observed in the base case (**C2**), with elevated values near the gas–liquid interface and within the wave body. For the $Re = 100$ and $Re = 200$ cases, the flow remains within the wavy-laminar regime [52], resulting in nearly identical hydrodynamic characteristics. Consequently, the dominant mechanisms responsible for pushing the liquid above its saturation limit — interfacial evaporation and internal recirculation — are all retained. However, because of higher viscous

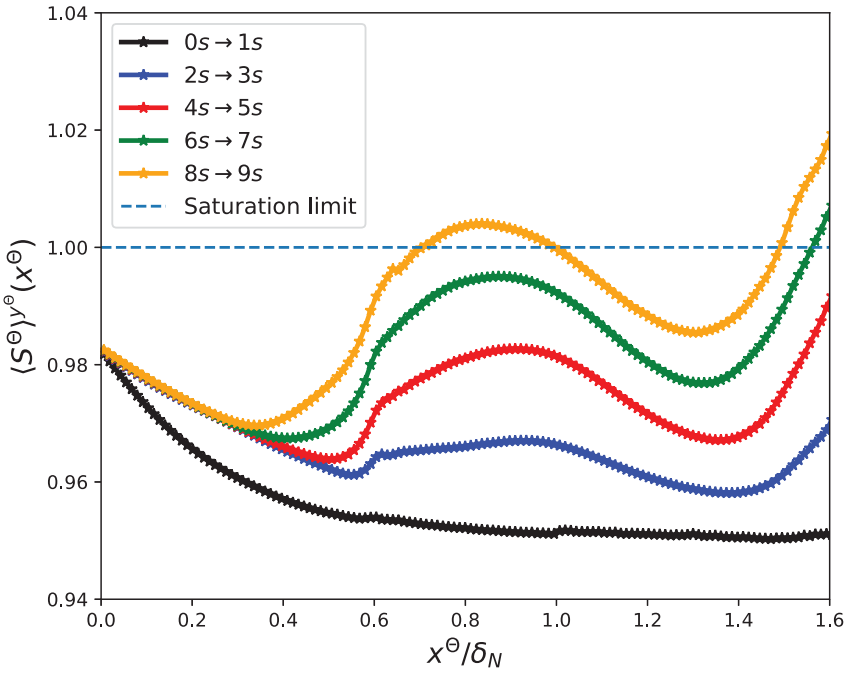

Fig. 10. Temporally and streamwise averaged non-dimensional supersaturation fields S^Θ in the liquid phase as a function of non-dimensional wall-normal distance for successive time intervals of the base case **C2**. Each curve corresponds to a distinct downstream section of the evaporator pipe. The dashed line marks the saturation threshold $S^\Theta = 1$. Supersaturation first occurs near the gas–liquid interface due to interfacial evaporation and later extends into the film interior as a result of hydrodynamic solute redistribution.

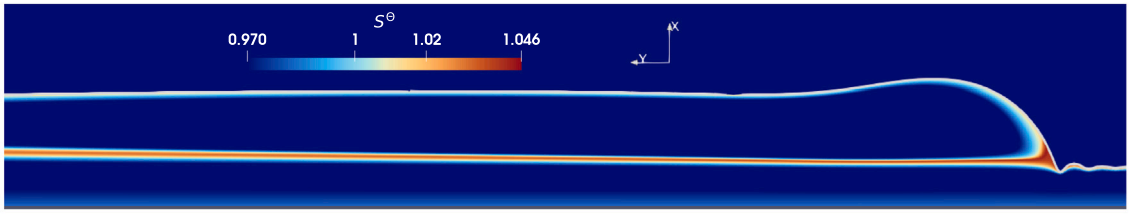

Fig. 11. Visualization of the non-dimensional supersaturation field S^Θ for the low Reynolds number case ($Re = 100$). The wave crest and the preceding capillary region are depicted, with the white line denoting the gas–liquid interface. Elevated supersaturation values are observed in the vicinity of the gas–liquid interface and within the mid-height region of the wave body.

forces at lower Reynolds numbers, coherent vortex structures within the wave body are less pronounced. Despite this, salt enrichment in the mid-height region is still observed, indicating that even relatively weak internal recirculation remains sufficient to redistribute the solute and support local supersaturation development.

Fig. 12 presents the scalar fields for the high Reynolds number case $Re = 400$ (**C3**), illustrating the non-dimensional quantities temperature T^Θ, salt concentration C^Θ_{salt}, and supersaturation S^Θ, distributed in the falling film. In subfigure (**a**), the temperature field T^Θ shows pronounced internal mixing and significant distortion of the thermal boundary layer, indicating enhanced convective transport and the breakdown of the coherent thermal stratification observed at lower Reynolds numbers, compare Fig. 5. The gas–liquid interface displays large-amplitude deformations and irregular wave structures, further promoting complex internal hydrodynamic motion. Subfigure (**b**) shows the salt concentration field C^Θ_{salt}, where strong internal vortical motions and highly filamented concentration structures are evident. Salt is no longer distributed smoothly across the film but is instead organized into complex, dynamically evolving patches, reflecting the dominant role of convective transport against purely diffusive processes. Subfigure (**c**) illustrates the supersaturation field S^Θ, which mirrors the chaotic salt distribution. Supersaturation levels are highly heterogeneous, with sharp local maxima appearing randomly throughout the film, both near the interface and within the bulk. This contrasts strongly with the more organized supersaturation patterns observed at $Re = 100$ and $Re = 200$, where supersaturation was mainly concentrated beneath the wave crest and near the gas–liquid interface.

To conclude our quantitative observations, Fig. 13 presents the non-dimensional, liquid-phase, temporally and streamwise averaged scalar fields T^Θ, C^Θ_{salt}, and S^Θ over the non-dimensional, normalized wall-normal coordinate x^Θ/δ_N for the Top, Middle, and Bottom regions at $Re = 400$. The temperature profiles remain qualitatively similar across all regions, indicating the persistence of a fully developed thermal boundary layer. However, in comparison with the lower Reynolds number cases, a slight reduction is observed in thermal gradients toward the gas–liquid interface, consistent with enhanced convective mixing at higher flow rates. The salt concentration fields C^Θ_{salt} exhibit a significant elevation throughout the entire film thickness, with progressive enrichment from the Top to the Bottom region. This indicates a strong influence of internal mixing and advection, leading to a more uniform and globally elevated solute distribution compared to the stratified profiles at lower Re. The supersaturation fields S^Θ reveal a corresponding shift, with values exceeding unity across a much broader region of the film. Supersaturation is no longer confined to narrow zones

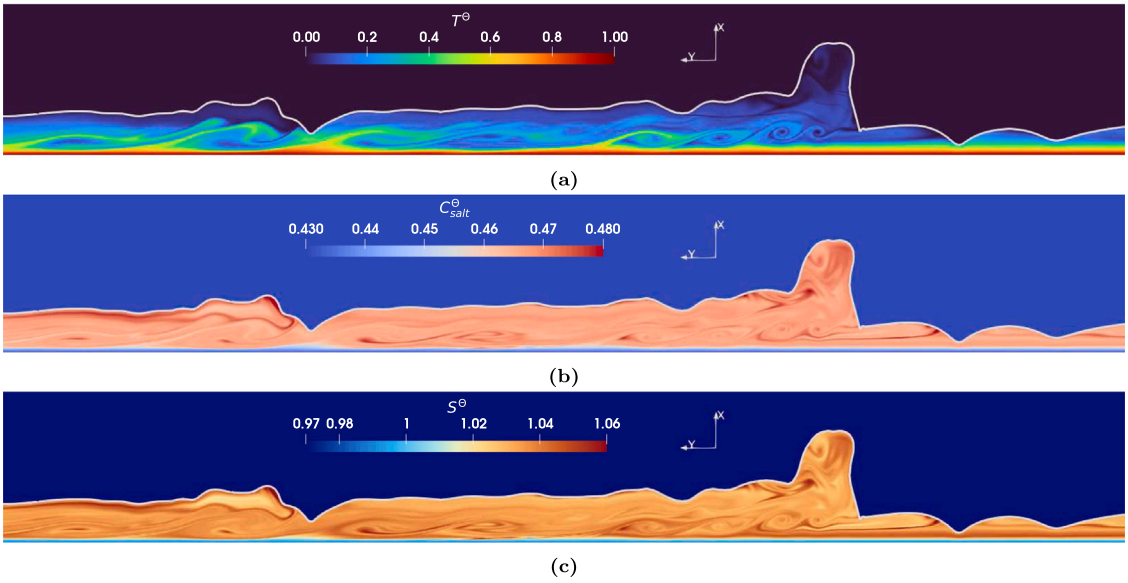

Fig. 12. The snapshots of zoomed-in scalar field distributions for the high Reynolds number case **C3** (Re = 400). (a) Non-dimensional temperature field T^{Θ}, showing significant disruption of the thermal boundary layer due to enhanced convective mixing. (b) Non-dimensional salt concentration field C^{Θ}_{salt}, exhibiting strong internal vortical structures and filamented concentration patterns. (c) Non-dimensional supersaturation field S^{Θ}, characterized by highly localized and irregular supersaturation regions. The visualizations reflect the transition to a chaotic wavy regime and the dominant role of convective transport at elevated Reynolds numbers. The white line in each subfigure represents the gas–liquid interface.

adjacent to the interface, but rather distributed throughout the bulk, driven by the enhanced solute transport and redistribution mechanisms. Taken together, these quantitative results corroborate the qualitative observations and underline the significant impact on supersaturation dynamics of increasing the Reynolds number. At Re = 400, the scalar transport is dominated by strong convective mixing and higher evaporative heat fluxes at the gas–liquid interface (compare with Fig. 4b), leading to widespread supersaturation across the film thickness. The strong redistribution of solute-rich fluid destabilizes the spatially organized supersaturation structures observed at lower Reynolds numbers, fundamentally altering the pathways for nucleation and crystallization.

3.6. Implications for falling film evaporators

The results of this study provide important insights for the design and operation of industrial falling film evaporators. One of the key findings is that higher Reynolds numbers, corresponding to increased wetting rates typical in industrial systems, are associated with a greater tendency for high supersaturation levels to develop near the heated wall. At these conditions, the flow becomes more chaotic and convectively dominated, which leads to a broader and less predictable distribution of supersaturated regions within the liquid film. This irregular transport makes it more difficult to control and locate the onset of crystallization fouling, increasing the likelihood of widespread deposit formation on internal surfaces. In contrast, at lower or moderate Reynolds numbers (belonging to the wavy laminar regime), supersaturation tends to follow more structured patterns governed by interfacial evaporation and flow-induced recirculation. These patterns, although more predictable, still pose potential fouling risk due to crystallization in the bulk and due to solute trapping and concentration build-up in specific zones. Importantly, both qualitative and quantitative data for **C2** and **C3** show that supersaturation tends to be higher near the bottom region of the evaporator pipe, especially close to the heated wall, which aligns with the experimental findings of Gourdon [45]. This is where longer residence times, internal recirculation, and solute transport from the gas–liquid interface toward the heated wall combine to create favorable conditions for crystallization. This observation is crucial for fouling control, as it highlights the lower sections of the evaporator as high-risk zones that may require targeted monitoring or cleaning strategies. Together, these findings emphasize that the Reynolds number (i.e. the wetting rate), interfacial evaporation, and inverse solubility effects must be carefully considered when evaluating fouling potential in falling film evaporators. Understanding where and how supersaturation forms provides a foundation for developing more effective mitigation strategies.

4. Conclusions

In this study, the mechanisms governing supersaturation dynamics in evaporating falling films were investigated through two-phase Direct Numerical Simulations. The primary aim was to identify where supersaturation emerges first and to analyze the mechanisms behind its spatial distribution in the film. We elucidated the interplay of interfacial evaporation, inverse salt solubility, and hydrodynamic effects in the appearance and evolution of supersaturated regions. A numerical framework based on the Volume of Fluid method was developed, featuring geometric reconstruction of the gas–liquid interface and a phase-based scalar transport modeling using geometrically computed fluxes and interface-based diffusion weighting. The framework was thoroughly validated against experimental, numerical, and analytical benchmarks, confirming its ability to fully resolve hydrodynamic- and heat-transfer phenomena in the film and reliably capture large-scale mass-transfer effects at high Schmidt numbers. Three Reynolds number cases (Re = 100, 200, and 400), representative of flow conditions in industrial evaporators used in the pulp and paper industry, were investigated. To simulate an industrially relevant evaporator pipe length of 10 m, we employ a spatial segmentation approach based on periodic boundary conditions, enabling the modeling of a physically long vertical falling film domain. The case with Re = 200 serves as the reference scenario throughout this study.

The results demonstrated that interfacial evaporation acts as the primary mechanism initiating supersaturation, driving initial solute enrichment near the gas–liquid interface. Flow separation and internal recirculation within the wave structures further promote solute trapping, leading to the formation of secondary supersaturated regions

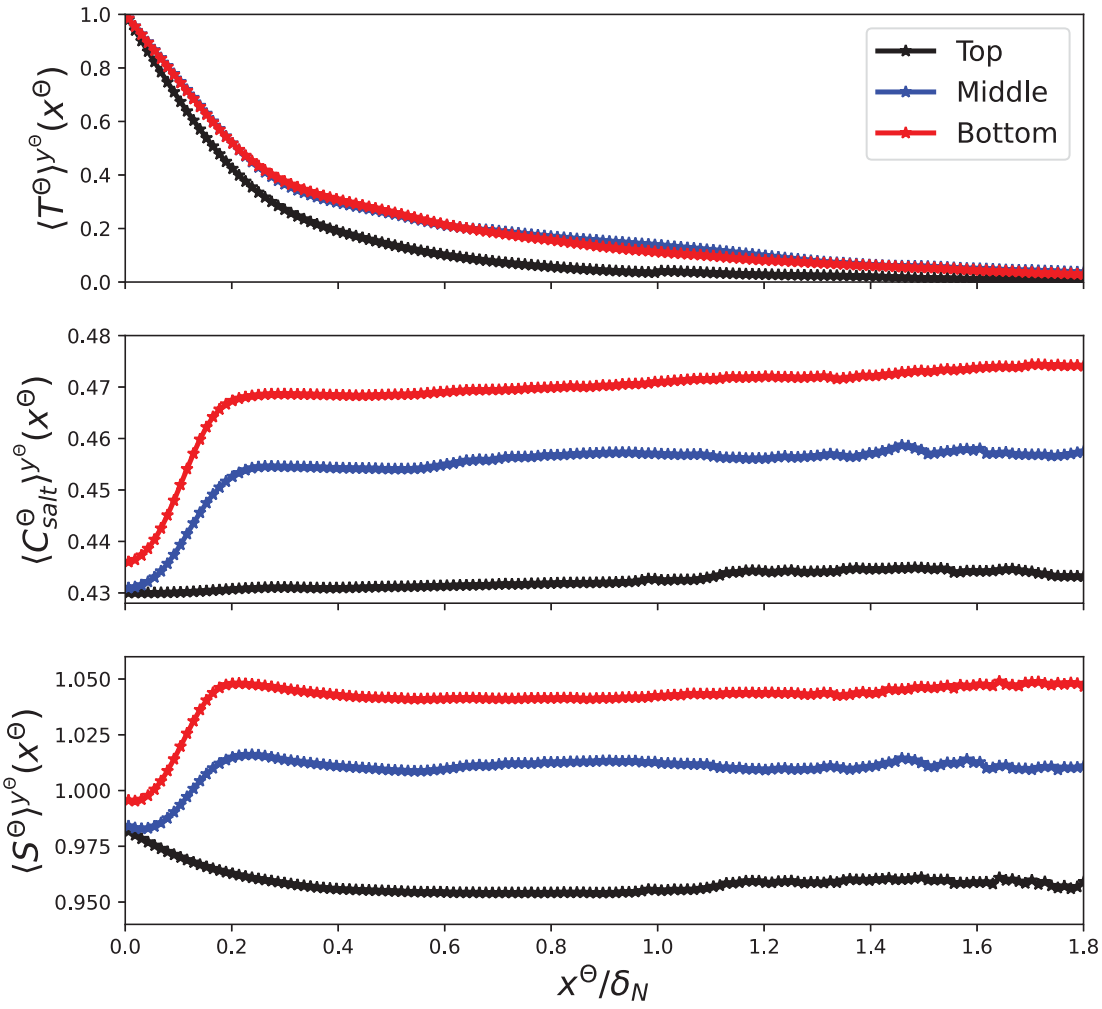

Fig. 13. Non-dimensional, liquid-phase temporally and streamwise averaged scalar fields for the high Reynolds number case $Re = 400$. (a) Temperature field T^Θ, (b) salt concentration field C^Θ_{salt}, and (c) supersaturation field S^Θ, plotted against the normalized wall-normal coordinate x^Θ/δ_N for the Top, Middle, and Bottom regions of the film. The results highlight the strong influence of convective mixing at elevated Reynolds numbers, leading to enhanced solute redistribution and widespread supersaturation throughout the film thickness. Compared to (Fig. 7**(b)**), an overall increase in salt concentration is observed, which we attribute to a higher evaporation rate in this case — potentially explaining the intensified solute accumulation.

within the film interior. The influence of inverse solubility becomes increasingly significant near the heated wall as residence times increase, since advection and diffusion will lead to solute concentration transport to the wall. A strong dependence of the supersaturation dynamics on the Reynolds number (linked to a film wetting rate) was observed: at $Re = 100$ and $Re = 200$, the flow exhibited organized supersaturation patterns influenced by interfacial transport and localized flow structures. In contrast, at $Re = 400$, the system transitioned to a more chaotic regime characterized by convectively dominated transport, leading to a widespread and irregular supersaturation distribution throughout the film. These findings provide new insights into the multiscale transport mechanisms underlying supersaturation in evaporating falling films and have important implications for the prediction and control of fouling and crystallization processes in industrial applications.

CRediT authorship contribution statement

D. Vleeschhouwers: Writing – review & editing, Writing – original draft, Visualization, Validation, Software, Methodology, Investigation, Formal analysis, Conceptualization. **N. Hidman:** Writing – review & editing, Visualization, Validation, Supervision, Software, Methodology, Formal analysis, Conceptualization. **H. Ström:** Writing – review & editing, Supervision, Methodology, Formal analysis. **S. Sasic:** Writing – review & editing, Supervision, Project administration, Methodology, Funding acquisition, Formal analysis, Conceptualization. **A. Åkesjö:** Conceptualization, Formal analysis, Supervision.

Declaration of competing interest

The authors declare that they have no known competing financial interests or personal relationships that could have appeared to influence the work reported in this paper.

Acknowledgments

Collaboration with, and the financial support of , the Resource-smart Processes Network financed by Vinnova via BioInnovation (2021-02078) and industrial partners (Billerud, SCA, Stora Enso, Södra Skogsägarna, and Valmet) is gratefully acknowledged. The computations were enabled by resources provided by the National Academic Infrastructure for Supercomputing in Sweden (NAISS), partially funded by the Swedish Research Council through grant agreement no. 2022-06725.

Data availability

Data will be made available on request.

References

[1] S. Kalliadasis, C. Ruyer-Quil, B. Scheid, M. Velarde, Falling Liquid Films, Applied Mathematical Sciences, Springer, 2012.
[2] J. Darand, A. Jafarian, Long-term simulation of crystallization fouling in a forced circulation crystallizer, Int. J. Heat Mass Transfer 231 (2024).
[3] A. Mersmann, Crystallization Technology Handbook, Marcel Dekker, Inc., 2001.
[4] B. Shi, Crystallization of solutes that lead to scale formation in black liquor evaporation (Ph.D. thesis), Georgia Institute of Technology, 2002.
[5] J. Berce, M. Zupancic, M. Moze, I. Golobic, A review of crystallization fouling in heat exchangers, Process. 9 (8) (2021).
[6] T. Pääkkönen, M. Riihimäki, C. Simonson, E. Muurinen, R. Keiski, Modeling $CaCO_3$ crystallization fouling on a heat exchanger surface - definition of fouling layer properties and model parameters, Int. J. Heat Mass Transfer 83 (2015) 84–98.
[7] T. Pääkkönen, U. Ojaniemi, T. Pättikangas, M. Manninen, E. Muurinen, R. Keiski, CFD modelling of $CaCO_3$ crystallization fouling on heat transfer surfaces, Int. J. Heat Mass Transfer 97 (2016) 618–630.
[8] H. Jin, S. Shahane, Y. Zhang, S. Wang, K. Nawaz, Modeling of crystallization fouling on a horizontal-tube falling-film evaporator for thermal desalination, Int. J. Heat Mass Transfer 178 (2021) 121596.
[9] M. Azimifar, A. Moradian, A. Jafarian, A numerical investigation on the dynamics of particle deposition and fouling on a vertical falling film pipe, J. Water Process. Eng. 66 (2024) 105990.
[10] G. Dietze, R. Kneer, Flow separation in falling liquid films, Front. Heat Mass Transf. 2 (2011) 033001.
[11] G. Dietze, On the kapitza instability and the generation of capillary waves, J. Fluid Mech. 789 (2016) 368–401.
[12] M. Gourdon, D. Strömblad, L. Olausson, L. Vamling, Scale formation and growth when evaporating black liquor with high carbonate to sulphate ratio, Nord. Pulp Pap. Res. J. 23 (2008).
[13] N. Hidman, A. Åkesjö, M. Gourdon, A. Jongsma, H. Ström, G. Sardina, S. Sasic, How surface modifications enhance vertical falling film evaporation, J. Fluid Mech. 997 (2024) 17–32.
[14] A. Åkesjö, M. Gourdon, L. Vamling, F. Innings, S. Sasic, Experimental and numerical study of heat transfer in a large-scale vertical falling film pilot unit, Int. J. Heat Mass Transfer 125 (2018) 53–65.
[15] F. Chen, Z. Gao, An analysis of black liquor falling film evaporation, Int. J. Heat Mass Transfer 47 (2003) 1657–1671.
[16] M. Gourdon, E. Karlsson, F. Innings, A. Jongsma, L. Vamling, Heat transfer for falling film evaporation of industrially relevant fluids up to very high Prandtl numbers, Heat Mass Transf. 52:379-391 (2015).
[17] P. Cyklis, Effect of fouling on falling film evaporator performance in industrial conditions of fruit juice concentrate production, J. Food Eng. 317, 110884 (2022).
[18] E. Doro, Computational Modeling of Falling Liquid Film Free Surface Evaporation (Ph.D. thesis), Georgia Institute of Technology, 2012.
[19] T. Adams, W. Frederick, T. Grace, M. Hupa, K. Lisa, A. Jones, H. Tran, Kraft Recovery Boilers, Tappi Press, American Forest and Paper Association, New York, 1997.
[20] G. Dietze, A. Leefken, R. Kneer, Investigation of the backflow phenomenon in falling liquid films, J. Fluid Mech. 595 (2008) 435–459.
[21] E. Doro, C. Aidun, Interfacial waves and the dynamics of backflow in falling liquid films, J. Fluid Mech. 726 (2013) 261–284.
[22] A. Åkesjö, M. Gourdon, L. Vamling, F. Innings, S. Sasic, Hydrodynamics of vertical falling films in a large-scale pilot unit - a combined experimental and numerical study, Int. J. Multiph. Flow 95 (2017) 188–198.
[23] G. Tryggvason, R. Scardovelli, S. Zaleski, Direct Numerical Simulations of Gas-Liquid Multiphase Flows, Cambridge University Press, 2011.
[24] S. Popinet, A quadtree-adaptive multigrid solver for the serre-green-naghdi equations, J. Comput. Phys. 302 (2015) 336–358.
[25] G. Dietze, Effect of wall corrugations on scalar transfer to a wavy falling liquid film, J. Fluid Mech. 859 (2019) 1098–1128.
[26] P. Farsoiya, S. Popinet, L. Deike, Bubble-mediated transfer of dilute gas in turbulence, J. Fluid Mech. 920 (2021) A34 1–21.
[27] W. Nusselt, Die oberflächenkondensation des wasserdampfes, VDI 50 (1916) 541–546.
[28] S. Popinet, Gerris: a tree-based adaptive solver for the incompressible Euler equations in complex geometries, J. Comput. Phys. 190 (2003) 572–600.
[29] J. Bell, P. Colella, H. Glaz, A second-order projection method for the incompressible Navier-Stokes equations, J. Comput. Phys. 85 (1989) 257–283.
[30] R. Scardovelli, S. Zaleski, Direct numerical simulation of free-surface and interfacial flows, Annn. Rev. Fluid Mech. 31 (1999) 567–603.
[31] S. Popinet, An accurate adaptive solver for surface-tension-driven interfacial flows, J. Comput. Phys. 228 (2009) 5838–5866.
[32] D. Bothe, S. Fleckenstein, A volume-of-fluid-based method for mass transfer processes at fluid particles, Chem. Eng. Sci. 101 (2013) 283–302.
[33] J. Berry, M. Davidson, H. D.J.E., A multiphase electrokinetic flow model for electrolytes with liquid/liquid interfaces, J. Comput. Phys. 251 (2013) 209–222.
[34] J. Lopez-Herrera, A. Ganan-Calvo, S. Popinet, M. Herrada, Electrokinetic effects in the breakup of electrified jets: A volume-of-fluid numerical study, Int. J. Multiph. Flow 71 (2015) 14–22.
[35] S. Popinet, Numerical models of surface tension, Annn. Rev. Fluid Mech. 50 (2018) 49–75.
[36] F. Denner, B. van Wachem, Numerical time-step restrictions as a result of capillary waves, J. Comput. Phys. 285 (2015) 24–40.
[37] C. Kunkelmann, Numerical Modeling and Investigation of Boiling Phenomena (Ph.D. thesis), Technische Universität Darmstadt, 2011.
[38] G. Schnabel, M3 Heat Transfer to Falling Films at Vertical Surfaces, VDI Heat Atlas, Springer, 2010.
[39] F. Gibou, L. Chen, D. Nguyen, S. Banerjee, A level set based sharp interface method for the multiphase incompressible Navier-Stokes equations with phase change, J. Comput. Phys. 222 (2007) 536–555.
[40] L. Malan, A. Malan, S. Zaleski, P. Rousseau, A geometric VOF method for interface resolved phase change and conservative thermal energy advection, J. Comput. Phys. 426 (2021) 109920.
[41] Y. Sato, B. Niceno, A sharp-interface phase change model for a mass-conservative interface tracking method, J. Comput. Phys. 249 (2013) 127–161.
[42] S. Hardt, F. Wondra, Evaporation model for interfacial flows based on a continuum-field representation of the source terms, J. Comput. Phys. 227 (2008) 5871–5895.
[43] R. Schrage, A Theoretical Study of Interphase Mass Transfer, Columbia University Press, 1953.
[44] A. Tourbier, L. Gamet, P. Beard, T. Michel, J. Aubin, H. Jasak, A consistent methodology to transport a passive scalar with the geometric volume-of-fluid method isoadvector, J. Comput. Phys. 513 (2024) 113198.
[45] M. Gourdon, Proceedings of international conference on heat exchanger fouling and cleaning, in: The Effects of Flow Velocity on Crystallization Fouling in Falling Film Black Liquor Evaporators, 2011.
[46] F. Denner, M. Pradas, A. Charogiannis, C. Markides, B. van Wachem, S. Kalliadasis, Self-similarity of solitary waves on inertia-dominated falling liquid films, Phys. Rev. E 93 (2016) 033121.
[47] A. Åkesjö, M. Gourdon, A. Jongsma, S. Sasic, Enhancing industrial vertical falling film evaporation through modification of heat transfer surfaces - an experimental study, Chem. Eng. Process. - Process. Intensif. 191 (2023) 109456.
[48] S. Hickel, N. Adams, On implicit subgrid-scale modeling in wall-bounded flows, Phys. Fluids 19 (2007) 105106.
[49] I. Calmet, J. Magnaudet, High-Schmidt number mass transfer through turbulent gas-liquid interfaces, Int. J. Heat Fluid Flow 19 (1998) 522–532.
[50] R. Numrich, Heat transfer in turbulent falling films, Chem. Eng. Technol. 18 (3), 171-177 (1995).
[51] J. Crank, The mathematics of diffusion, Clarendon Press Oxford, 1975.
[52] F. Al-Sibai, Experimentelle Untersuchung der Strömungscharakteristik und des Wärmeübergangs bei welligen Rieselfilmen (Ph.D. thesis), RWTH Aachen University, 2004.